nature communications

Article

https://doi.org/10.1038/s41467-026-77268-8

Lipid network crosslinked hydrogels control material dynamics across multiple length scales through lipid movement

Received: 22 January 2026

Accepted: 20 August 2026

Published online: 27 August 2026

Check for updates

Neil J. Baugh[1], Michelle S. Huang[2,3], Narelli de Paiva Narciso[1], Jordan A. Bunch[1], Jayniana Williams[1], Daiyao Zhang[2], Vanessa M. Doulames[1], Yueming Liu[1], Ruby Onsongo[1], David Kilian[1,4], Renato S. Navarro[1,5] & Sarah C. Heilshorn[1,3]

Control over network dynamics across length scales is a feature of natural materials challenging to replicate in synthetic hydrogels. Taking inspiration from biological materials that feature lipids as structural elements, we introduce Lipid Network Crosslinked (LINC) hydrogels that exploit the mobility of individual lipids within self-assembled liposomes as covalent, network-crosslinking points. These mobile, covalent crosslinks increase hydrogel stress relaxation rates over 20-fold compared to polymer-only hydrogels with equivalent stiffness. Liposome design parameters, including degree of surface functionalization and tail saturation, provide a means to independently control the macroscale storage moduli and stress relaxation behavior. Finally, we place cell-adhesive ligands onto more mobile or less mobile network elements. Human neural progenitor cells within LINC hydrogels significantly alter their phenotype in response to nanoscale ligand dynamics. These results establish LINC hydrogels as biomimetic materials that leverage nanoscale lipid mobility within a macroscale polymeric network to control dynamics at multiple length scales.

Native tissues have distinct time scales of motion at different length scales due to their hierarchical network structure that includes both lipids and polymers. At the macroscale, the extracellular matrix exhibits viscoelastic mechanical properties[1–3]. At the nanoscale, the dynamics are dictated by the molecular mobility of individual network components, including the lipids within the cell membrane[4,5]. Recapitulating these multi-length scale dynamics in engineered materials remains a major challenge, as it is difficult to independently tune macroscale viscoelasticity and nanoscale mobility.

Viscoelastic hydrogels have a broad range of healthcare-related applications, including as scaffolds for tissue engineering, delivery devices for regenerative medicine, and extrudable inks for 3D printing[6–10]. Conventional viscoelastic hydrogels are formed by a network of polymers with reversible crosslinks, such as dynamic covalent chemistry (DCC) bonds or non-covalent interactions[6,11–13]. These materials enable tuning of macroscale dynamics through control of molecular-level properties, including crosslink density and bond dynamics. In these systems, the macroscale stress relaxation rate is governed by the crosslink kinetics, which dictate nanoscale polymer mobility as the crosslinks reversibly detach and reform[14,15]. Alternatively, supramolecular assemblies can also form viscoelastic structural hydrogels[7,11,16,17]. Although nanoscale dynamics in supramolecular gels can be tuned through careful design, because these systems typically form larger length scale networks through entanglements of

[1]Department of Materials Science and Engineering, Stanford University, Stanford, CA, USA. [2]Department of Chemical Engineering, Stanford University, Stanford, CA, USA. [3]The Institute for Chemistry, Engineering & Medicine for Human Health (Sarafan ChEM-H), Stanford University, Stanford, CA, USA. [4]Department of Complex Tissue Regeneration, MERLN Institute for Technology-Inspired Regenerative Medicine, Maastricht University, Maastricht, The Netherlands. [5]Department of Materials Science and Engineering, University of Florida, Gainesville, FL, USA. e-mail: heilshorn@stanford.edu

the individual matrix components, they typically lack independent control over macroscale dynamics[17–19]. Recently, there has been increased interest in decoupling nano- and macroscale dynamics in viscoelastic hydrogels. For instance, interpenetrating networks of covalently crosslinked polyethylene glycol and supramolecular self-assembled peptide amphiphiles (PA) revealed that endothelial cell spreading is influenced by macroscale gel properties (stiffness, stress relaxation) and nanoscale bioactive ligand mobility[19]. Others have leveraged combinations of discrete peptide building blocks within PA hydrogels to independently control molecular and network-level properties and found that fibroblasts respond to these multi-lengthscale dynamics[20,21]. These recent works highlight the broader emerging framework that decoupling bulk mechanics from molecular-scale mobility can significantly impact cell-material interactions.

Taking inspiration from natural tissues, we sought to leverage the mobility of lipids to design hydrogels with control over both macroscale and nanoscale dynamics. Lipids retain their nanoscale mobility upon self-assembly into larger structures[4,5,22], providing an attractive starting point to generate materials with tunable, multi-length scale dynamics. Lipid self-assembly is ubiquitous in naturally evolved systems, and while lipid-based particles are commonly used in hydrogel drug delivery[23–26], they have been overlooked as structural elements in hydrogel design. In certain conditions, lipids will spontaneously self-assemble into large lipid-rich domains in aqueous solvents[27], but do not form hydrogels without external bonding. At high concentrations, self-assembled lipids can form supramolecular hydrogels when combined with polymers containing hydrophobic pendants[28], fatty acids[29], or nucleotide modifications[30]. However, due to weak hydrophobic interactions, these materials have limited mechanical properties and do not have multi-length-scale dynamic control. Here, we introduce a structural hydrogel composed of nanoscale, self-assembled lipids that are covalently crosslinked into larger, macroscale, polymeric networks. This hierarchical design offers multi-length-scale control of network dynamics, resulting in hydrogels with tunable macroscale viscoelasticity and nanoscale mobility.

Specifically, we design a supramolecular, Lipid Network Crosslinked (LINC) hydrogel, in which liposomes are covalently crosslinked to hyaluronic acid (HA) polymers through individual, mobile lipids (Fig. 1a). This design allows for the presentation of lipid-tethered active elements (e.g., crosslinking ligands or cell-adhesive ligands) with tunable control over nanoscale dynamics in the mobile lipid bilayer (Fig. 1b). We hypothesized that crosslinking the polymeric network through individual lipid-ligands would facilitate control over macroscale network dynamics, including stress relaxation behavior (Fig. 1c). This design strategy exploits the structure-function relationships between lipid physicochemical properties and self-assembled membrane fluidity, providing a method to control hydrogel properties at both the nano- and macroscales. To validate this design strategy, we use fluorescence measurements of nanoscale lipid mobility and relate them to macroscale measurements of network rheology. This modular design flexibility enabled the formulation of hydrogels with a wide range of stiffnesses (shear moduli G' spanning about 100–2000 Pa) and stress relaxation rates (relaxation half-lives spanning about 30 min to 24 h). Importantly, we find that mobile crosslinking ligands increase

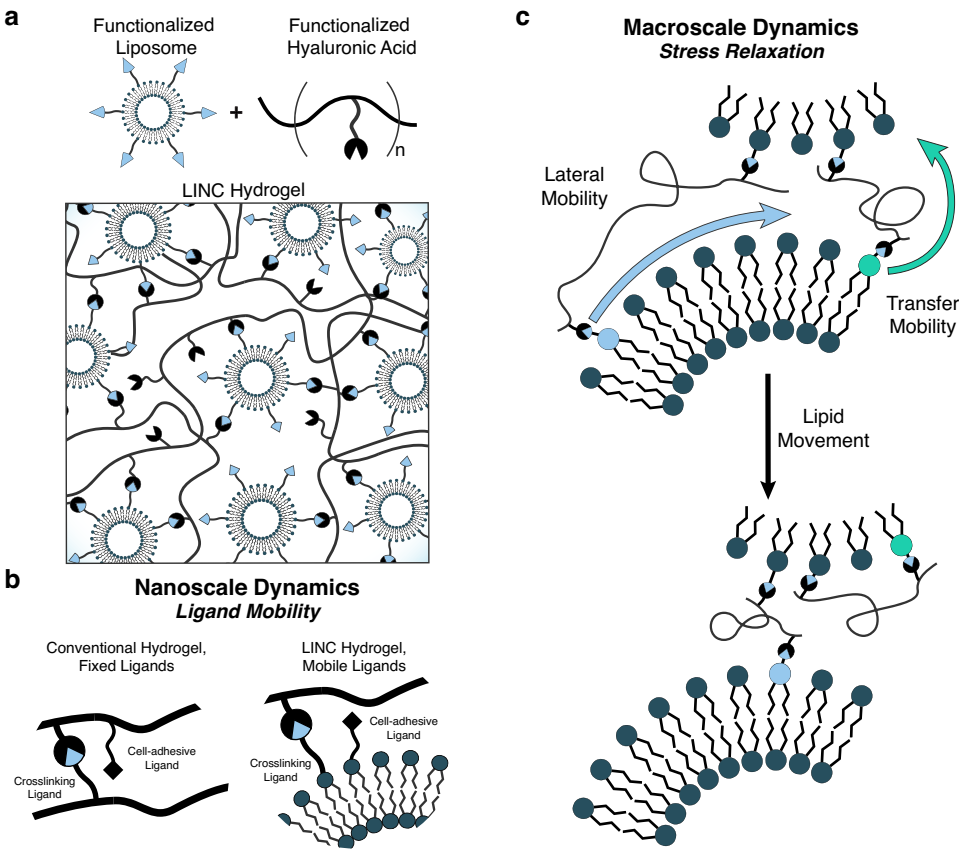


Fig. 1 | Lipid Network Crosslinked (LINC) hydrogels. a Self-assembled liposomes present covalent crosslinking ligands to form a network of hyaluronic acid (HA) biopolymers. This design is termed LINC hydrogel. **b** Unlike conventional viscoelastic hydrogels where functional ligands are fixed to the polymer backbone, LINC hydrogels offer control over nanoscale dynamics by tethering ligands to the mobile lipid bilayer. Examples of functional ligands include crosslinking functional groups (circles) or cell-adhesive peptides (black diamonds). **c** Due to both the lateral mobility and transfer mobility of the lipid-tethered crosslinking ligands, LINC hydrogels readily relax in response to applied stress, offering control over macroscale network dynamics.

https://doi.org/10.1038/s41467-026-77268-8

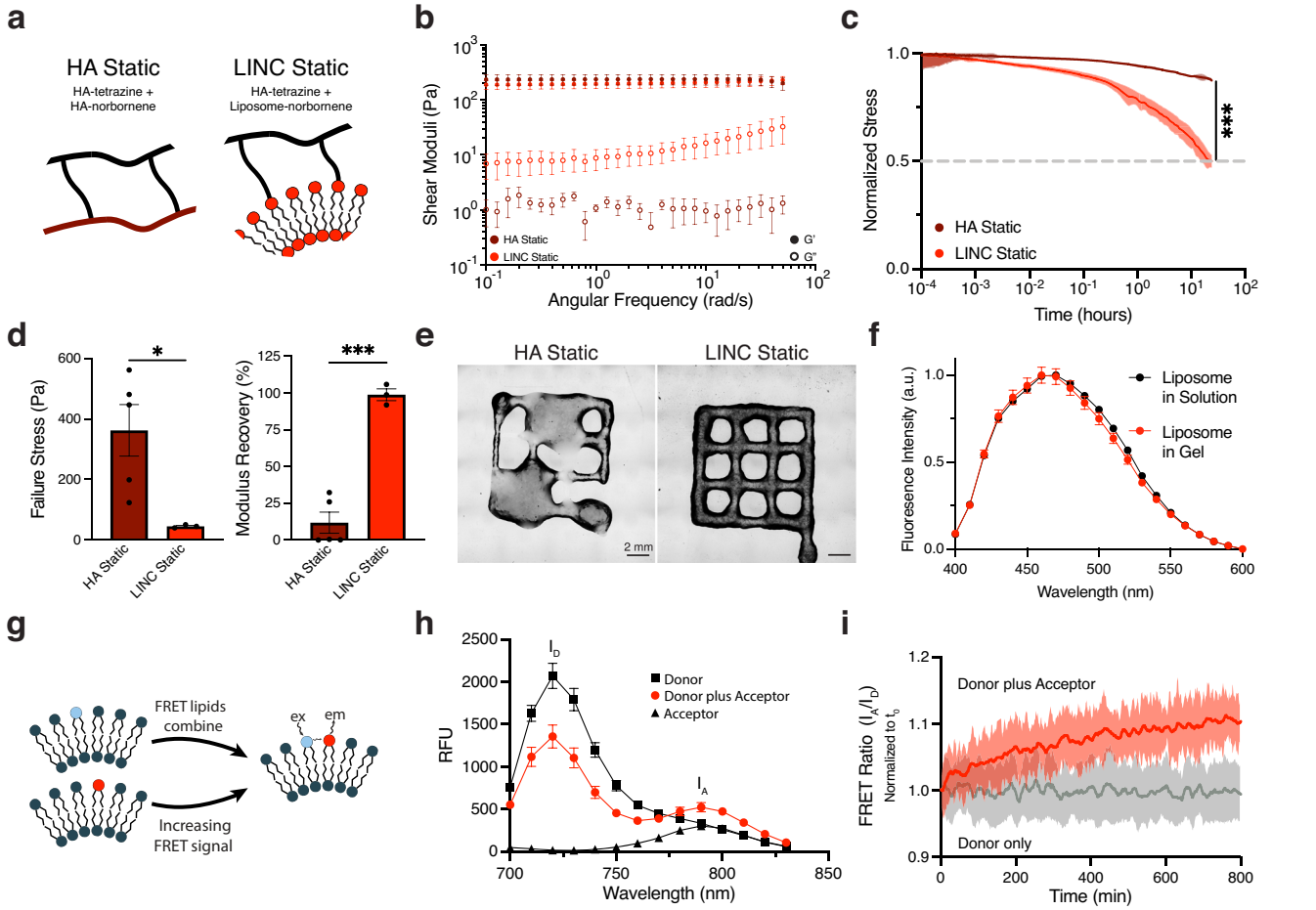


Fig. 2 | Lipid mobility generates stress relaxation despite irreversible crosslinking in static covalent LINC gels. a Schematic of HA-only gel (HA-tetrazine + HA-norbornene) and LINC gel (HA-tetrazine + liposome-norbornene) with static covalent crosslinks. **b** Rheology frequency sweeps of LINC Static and HA Static gels. Shear storage (G') and loss (G'') moduli are filled and open symbols, respectively (LINC $N = 3$, HA $N = 5$ independent replicates, mean ± standard deviation). **c** Normalized stress relaxation of LINC Static and HA Static gels ($N = 3$ independent replicates, mean ± standard deviation, $^{***}p = 0.0003$ at 24 h, two-tailed unpaired t test). **d** Failure stress and plateau shear storage modulus recovery post-failure (LINC $N = 3$, HA $N = 5$, data is mean ± standard deviation, $^{*}p = 0.0313$, $^{***}p = 0.0001$, two-tailed unpaired t tests). **e** 3D printing of "open window" lattice tests. The lipid mobility significantly increases the yielding behavior and the ability to recover mechanical properties after yielding, thus making the gels printable. **f** LAURDAN emission spectra for liposomes in solution (black) and crosslinked into LINC Static gels (red) showing the lipid membrane maintains fluidity when crosslinked ($N = 3$, data are mean ± standard deviation). **g** Schematic of FRET experiment showing lipid transfer across liposomes. **h** Fluorescence spectra of donor only, acceptor only, and donor plus acceptor LINC Static gels taken at the end of the assay in (**i**) ($N = 3$ independent replicates, mean ± standard deviation). **i** Increasing FRET ratio over time confirms lipid transfer between liposomes, compared to the donor-only control ($N = 3$ independent replicates, mean ± standard deviation). Source data are provided as a Source data file.

hydrogel stress relaxation rates over 20-fold compared to polymer-only hydrogels with equivalent crosslinking chemistries and stiffnesses. Finally, we demonstrate that control over network dynamics at different length scales is critical in engineering cell morphology. By placing cell-adhesive ligands onto the more mobile lipid bilayers or less mobile polymer network, we show that human neural progenitor cells (hNPCs) cultured within LINC hydrogels of identical macroscale viscoelasticity significantly altered their morphology in response to nanoscale ligand dynamics. Here, we establish LINC hydrogels as biomimetic materials that leverage nanoscale lipid mobility within a macroscale polymeric network to control dynamics at multiple length scales.

Results and discussion

Covalent LINC gels enable control of macroscale stress relaxation

We hypothesized that the dynamic nature of lipid self-assembly would afford stress relaxation properties to covalently crosslinked gels, which typically would be quasi-elastic due to their permanent crosslinking points[6]. To test this, we formulated LINC gels with permanent, static covalent bonds between an HA biopolymer and self-assembled liposomes using norbornene and tetrazine functional groups (termed LINC Static, Figs. 2a and S1). We fabricated 100-nm liposomes using the commonly employed thin-film hydration and sonication method (Figs. S2 and S3). First, lipids dissolved in chloroform were mixed at the desired ratios and dried to remove excess chloroform (DOPC:DOPE-maleimide, 92:8 mol%, Table S1). The resulting lipid films were hydrated in PBS, collected, and sonicated until 100-nm liposomes were obtained. Then, liposomes were surface functionalized with crosslinking groups by reacting the DOPE-maleimide lipids with an excess of thiol/norbornene bifunctional polyethylene glycol. Finally, the norbornene-functionalized liposomes were purified and concentrated before use. When mixed, norbornene-functionalized liposomes and tetrazine-functionalized HA spontaneously crosslink to form a hydrogel (Fig. S4). As a comparative control, we synthesized a conventional hydrogel composed only of HA-tetrazine and HA-norbornene (termed HA Static, Fig. 2a). These HA Static gels had identical crosslinking chemistry, total HA concentration

(1 wt%), HA-tetrazine functionalization (8%, Fig. S1), and similar stiffness (plateau shear storage modulus, G' ~ 200 Pa; Fig. 2b) to LINC Static gels (Table S2).

Consistent with literature on chemical hydrogels[6,15], HA Static gels demonstrated limited stress relaxation, appearing quasi-elastic over 24 h. In contrast, LINC Static hydrogels reached 22% relaxation after only 1 h and 50% relaxation after 24 h (Fig. 2c). Furthermore, LINC Static gels exhibited lower failure stress and greater recovery post-failure, making them injectable and suitable as inks for extrusion-based 3D printing, while HA Static gels were unable to be printed (Figs. 2d, e and S5). These differences likely derive from the relatively weaker crosslinking strength in the LINC Static gels, which rely on physical lipid-lipid interactions, compared to the stronger covalent crosslinks in HA Static gels. As the LINC Static gels are deformed, the crosslinking lipids are likely pulled out of the liposomal membrane prior to covalent bond failure.

To test the durability of the observed stress relaxation behavior, we conducted oscillatory strain-amplitude sweeps until the LINC Static gels failed and subsequently recovered over 2 h (Fig. S6). Notably, we found that the LINC Static gels exhibited similar relaxation behavior pre-failure and post-failure, suggesting that the lipid-crosslinked network is able to recover. LINC Static gels presented higher loss moduli than HA Static gels at every measured frequency, indicating a larger viscous contribution (Fig. 2b). This suggests that lipid mobility within the self-assembled liposomes enables viscous dissipation in LINC gels despite the irreversibility of the static covalent crosslinking. Thus, the network harnesses the molecular motion of individual lipids to enable network-level stress relaxation.

Lipids maintain nanoscale mobility in LINC gels

We reasoned that the self-assembled lipids could contribute to viscous dissipation and macroscale stress relaxation through two different modes: (i) lateral mobility within the membrane of a single liposome and (ii) transfer mobility from one liposome to another (Fig. 1c). Both motions would enable the covalently-bound HA chains to reorient and dissipate applied stress. To confirm both modes of lipid movement occur in LINC gels, we first compared the overall membrane fluidity of liposomes in solution to those crosslinked into a gel. The fluorescent dyes 6-acetyl-2-dimethylaminonaphthalene (ACDAN) and 6-dodecanoyl-2-dimethylaminonaphthalene (LAURDAN) are sensitive to local water, which correlates with lipid membrane fluidity[31,32]. The fluorescence of ACDAN, which positions itself closer to the water interface, and for LAURDAN, which partitions further into the lipid bilayer due to a longer acyl tail, were similar for liposomes in solution and those in LINC gels, suggesting the overall membrane fluidity is retained after network crosslinking (Figs. 2f and S7).

After confirming that lipid membrane hydration, which correlates with membrane fluidity, is maintained after being crosslinked into a hydrogel, we next examined potential nanoscale lipid movement between liposomes using Förster Resonance Energy Transfer (FRET) (Fig. 2g–i). Liposomes labeled only with donor dye (Cy5.5) or only with acceptor dye (Cy7) were mixed with functionalized HA to create a LINC Static gel (Fig. 2g). Upon excitation of the donor, the FRET signal increased over time as individual lipids transferred into the same liposomes, moving the donors and acceptors close together (Förster radius ~5–7 nm[33,34], Fig. 2h, i). As expected, no changes were observed in donor-only and acceptor-only controls (Figs. 2i and S8a). To help rule out contributions from mobile, uncrosslinked liposomes, we measured the change in FRET Ratio of liposomes in solution at comparable concentrations and saw no change in fluorescence (Fig. S8b). This indicates that lipid transfer is significantly increased for network-bound liposomes, potentially through prolonged particle confinement in close proximity and/or local stress and strain at the lipid interface, enabling greater lipid exchange between crosslinked liposomes compared to those in solution. As additional evidence of lipid transfer across network-bound liposomes within LINC Static gels, we prepared materials using a mixture of liposomes with no labeled lipids and liposomes containing both donor and acceptor fluorophore labels (Fig. S8b). Over time, we observed a decrease in FRET signal, indicating that the initially colocalized donor-acceptor lipids became more dispersed as they transferred into the unlabeled liposomes (Fig. S8d, e). Overall, these results suggest that lipids maintain their membrane mobility and can transfer to nearby liposomes while crosslinked into larger polymeric networks, validating the hierarchical, biomimetic design strategy.

Dynamic covalent LINC gels exhibit tunable macroscale viscoelasticity

To demonstrate versatility in these hierarchical materials, we next modified the crosslinking ligands to enable dynamic covalent chemistry (DCC) crosslinking as an alternative to static covalent crosslinking. DCC crosslinking has emerged as a strategy to design chemical hydrogels with tunable control of macroscale stress relaxation rates; however, these systems typically have relatively slow stress relaxation half-lives compared to hydrogels with non-covalent crosslinks[12,35]. We reasoned that combining DCC with the lipid mobility of LINC gels would result in rapidly stress-relaxing gels due to combined contributions from both the chemical crosslinks and lipid movement. To test this idea, we modified HA biopolymers with a benzaldehyde motif as previously described[15]. Liposomes were decorated with hydrazine groups that react with benzaldehyde to form a dynamic covalent hydrazone bond with appreciable on- and off-rates at physiological conditions[12,36,37].

We compared the viscoelasticity of these hydrazone-crosslinked gels (termed LINC Dynamic) to HA-only hydrogels (termed HA Dynamic) prepared with the same DCC crosslinks (Figs. 3a and S9–S11). After mixing benzaldehyde-modified HA with either hydrazine-modified HA or hydrazine-modified liposomes, hydrogels rapidly formed within 5–10 s (Fig. S4). As before, the degree of modification was selected to achieve similar gel stiffness (G' ~ 200 Pa) with an equivalent concentration of HA (1 wt%) (Fig. 3b). Both HA Dynamic and LINC Dynamic formulations displayed shear-thinning, self-healing, and strain-stiffening behavior, which are common in DCC crosslinked gels (Fig. S12)[38]. Importantly, upon application of a step strain, the HA Dynamic gels exhibited a stress relaxation half-life ($t_{1/2}$) of 14.2 h, while $t_{1/2}$ for LINC Dynamic gels was an order of magnitude faster at 1.2 h (Fig. 3c). In conventional DCC hydrogels, polymer chains move when the dynamic bonds are off to dissipate stress, making stress relaxation dependent on crosslinking reaction kinetics[35]. Here, by combining lipid mobility with reversible covalent crosslinking, we achieved a ~12-fold increase in stress relaxation rate despite identical crosslinking chemistry.

Interestingly, while the HA Static and HA Dynamic gels had similar loss moduli (G'' ~ 1 Pa), the LINC Static gels displayed significantly higher loss moduli than LINC Dynamic gels (G'' ~ 10 vs 1 Pa, respectively) (Figs. 2b and 3b). These data suggest that at the relatively short timescales examined by shear rheology, viscous dissipation in the HA-only gels occurs primarily through movement of the HA chains, regardless of the crosslinking chemistry. In contrast, for LINC Static gels, increased viscous dampening occurs, presumably through lipid mobility. Surprisingly, for the LINC Dynamic gels, which are capable of molecular motion through both lipid mobility and hydrazone bond exchange, the lower loss modulus suggests greater energy storage at short timescales compared to the LINC Static gels, despite their significantly faster stress relaxation half-life of 1.2 h. This discrepancy suggests that the combination of lipid mobility and crosslink exchange can have different, non-additive effects at different time scales. For example, network crosslinking may result in altered lipid mobility. Alternatively, the presence of lipids may alter the hydrazone exchange kinetics, which are known to be sensitive to local pH and ionic

https://doi.org/10.1038/s41467-026-77268-8

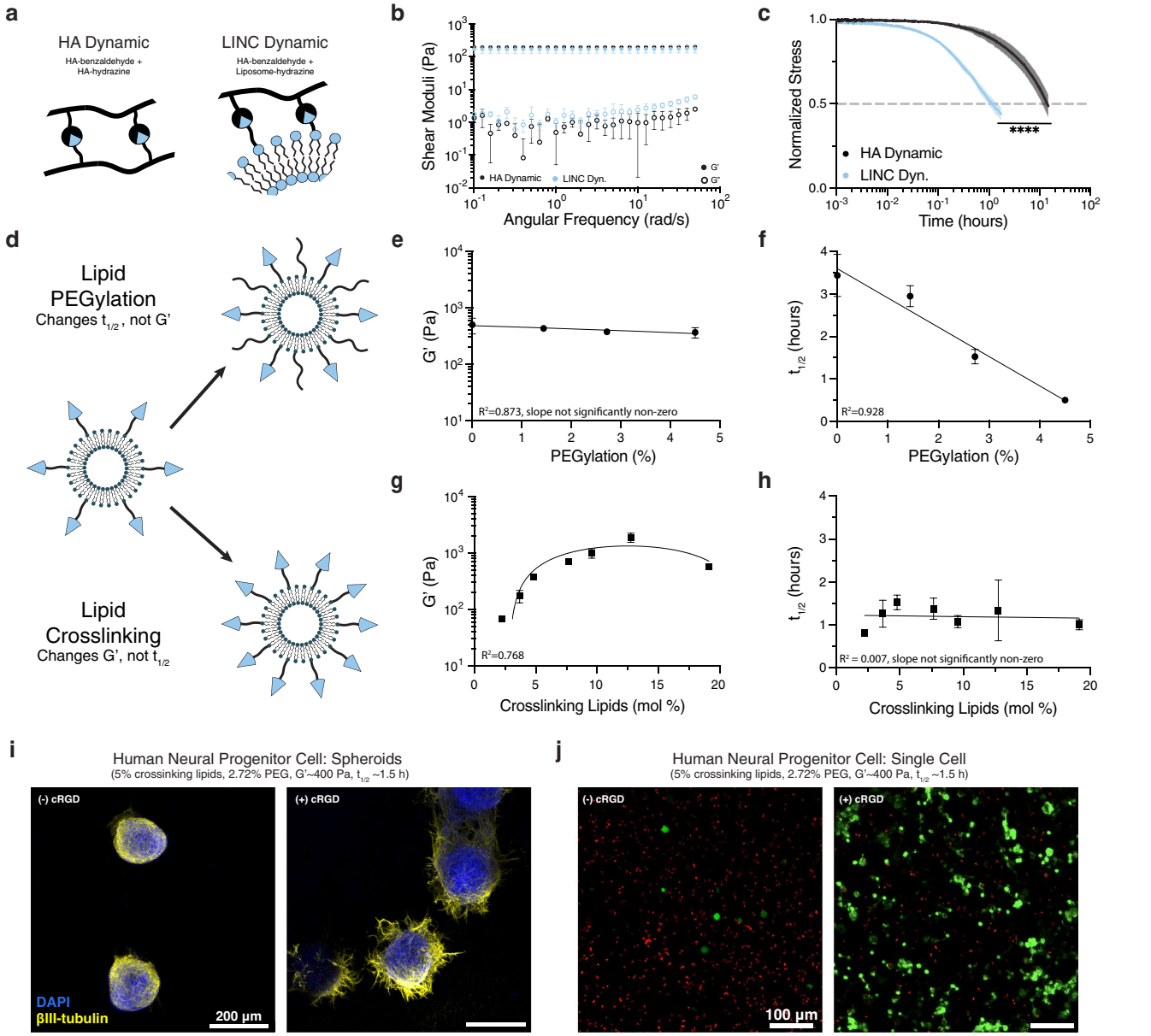


Fig. 3 | Combining lipid mobility with dynamic covalent crosslinking results in tunable viscoelasticity. a Schematic of HA-only (HA-benzaldehyde + HA-hydrazine) and LINC gels (HA-benzaldehyde + liposome-hydrazine) with dynamic covalent crosslinks. **b** Rheology frequency sweeps of LINC Dynamic and HA Dynamic gels. Shear storage (G') and loss (G'') moduli are filled and open symbols, respectively ($N = 3$ independent replicates per condition, mean ± standard deviation). **c** Normalized stress relaxation of LINC Dynamic and HA Dynamic gels ($N = 3$ independent replicates, $^{****}p < 0.0001$, two-tailed unpaired t test). **d** Schematic showing control of LINC gel viscoelasticity through modifying liposome PEGylation (top) or crosslinking density (bottom). The resulting storage modulus (**e**) and $t_{1/2}$ (**f**) of LINC Dynamic gels with increasing PEGylation. ($N = 3$ independent replicates per condition, fits are linear regressions). The resulting storage modulus (**g**) and $t_{1/2}$ (**h**) of LINC Dynamic gels with increasing crosslinker functionalization ($N = 3$ for 2.2-9.6 mol%, $N = 5$ for 12.8 mol%, $N = 2$ for 19.1 mol%, fits are quadratic (**g**) and linear regression (**h**)). All comparisons in (**e**, **h**) not statistically significant ($p \geq 0.32$ (e); $p \geq 0.27$ (**h**)) using ordinary one-way ANOVA with Tukey's multiple comparison test. **i** Human neural progenitor cells cultured as spheroids (**i**) or single cells (**j**) for 7 days in LINC Dynamic gels (4.7% crosslinking lipids, 2.72% PEGylated lipids, G' ~ 400 Pa, $t_{1/2}$ ~ 1 h) without (left) and with (right) lipid-anchored cRGD. **i**, **j** were repeated 3 times with similar results. Scale bar is 200 μm (**i**) or 100 μm (**j**). All data are mean ± standard deviation. Source data are provided as a Source data file.

concentration[39,40]. Incorporating uncrosslinked liposomes within the HA Dynamic gels had no statistically significant effect on either gel stiffness or stress relaxation rate (Fig. S13), suggesting limited changes in hydrazone exchange kinetics from the presence of uncrosslinked lipids alone.

Within the LINC gels, the relatively rapid, molecular-level interactions (i.e., lipid mobility and crosslink exchange) are geometrically connected into a larger length-scale network that displays a macroscale stress-relaxation rate over minutes to hours. Altogether, we demonstrate that lipid-crosslinked networks display significantly faster stress-relaxation rates compared to polymer-only networks, both for static and dynamic covalent chemistries (Figs. 2c and 3c).

We next explored strategies to tune the viscoelastic properties of LINC hydrogels through liposome design (Fig. 3d). We hypothesized that displaying polyethylene glycol (PEG) from the liposome surface would modulate lipid mobility, and hence stress relaxation rate, without impacting the degree of crosslinking. Separately, we hypothesized that altering the concentration of crosslinking lipids would tune the resulting gel stiffness without impacting lipid mobility. When

combined, these two strategies allow us to precisely control the viscoelastic properties of LINC gels.

To test the first hypothesis, we varied the fraction of PEGylated lipids, which has been reported to increase lipid membrane fluidity in some conditions[41], while holding the amount of hydrazine functionalization approximately constant. The resulting LINC gels all had similar stiffness (G' ~ 400 Pa) (Figs. 3e and S14), suggesting that the presence of PEG did not disrupt hydrazone crosslinking. Increasing PEGylation allowed for faster stress relaxation rates, with an inverse linear relationship between $t_{1/2}$ and the percentage of PEGylated lipids ($R^2 = 0.928$) (Figs. 3f and S15). Compared to LINC Dynamic gels without PEGylation, adding PEG to 4.5% of lipids decreased $t_{1/2}$ by about one order of magnitude to 30 min, ~20-fold faster than the HA Dynamic gels (Fig. 3f) and approaching reported values of soft tissues[3,42]. As discussed above, viscous dissipation in LINC Dynamic gels is a consequence of both lipid mobility and hydrazone bond exchange. Thus, the observed faster stress relaxation rates could be a consequence of increased lipid mobility and/or increased hydrazone bond kinetics. Future mechanistic studies will be required to elucidate how the presence of PEG influences both of these dynamic processes.

To test the second hypothesis, we fixed the PEGylation-to-hydrazine ratio and varied the concentration of hydrazines available for crosslinking. A maximum stiffness (G′) of ~1900 Pa was achieved for LINC Dynamic gels with 12.75 mol% crosslinking lipids (Fig. 3g). Further increases in crosslinking lipid resulted in lower stiffness, potentially due to network defects in connectivity, such as HA binding to individual liposomes instead of bridging across them, or percolation effects. Importantly, the $t_{1/2}$ stayed largely constant for all gel formulations (Fig. 3h), despite the storage modulus changing by an order of magnitude. Thus, by leveraging the nanoscale design of the liposome lipid bilayers, we were able to independently tune the hydrogel stiffness and the stress relaxation rate, which is difficult to achieve with conventional chemical gels without modifying crosslinking chemistry.

Tunable control of hydrogel mechanical properties is particularly helpful when designing in vitro models of human tissues[3,15,36], so we next explored if these materials could serve as scaffolds to support the growth of 3D cultures. Human pluripotent stem cell-derived tissue models, such as single-cell cultures, spheroids, and organoids, are increasingly used to recapitulate native tissues and elucidate mechanisms of development, disease, and therapeutic drug effects[43,44]. To demonstrate the modularity and cytocompatibility of the LINC Dynamic platform, we formulated gels to have stiffnesses known to be supportive of human neural progenitor cells (hNPCs) spheroids or hepatic progenitor organoids, G' ~ 400 or 1000 Pa, respectively[45,46]. To engage with integrin cell-surface receptors, we designed the liposomes to present lipid-anchored, cell-adhesive ligands (Fig. 1b). Specifically, we functionalized lipids with cyclic RGD (cRGD) peptides, a common cell-adhesive ligand that mimics an integrin epitope found in the native extracellular matrix[47]. To confirm bioactivity of cRGD-presenting liposomes, induced pluripotent stem cell-derived hNPCs were encapsulated as spheroids in LINC Dynamic gels with and without the cRGD ligand (1.5 and 0 mM cRGD, respectively). Without cRGD, hNPC spheroids failed to extend βIII-tubulin-positive neurites, while spheroids in LINC Dynamic gels with lipid-anchored cRGD exhibited robust neurite extension (Figs. 3i and S16). To eliminate potential confounding cell-cell interactions, hNPCs were cultured as single cells in the same gel conditions. Without cRGD, single-cell hNPCs exhibited low viability and minimal projections compared to those in LINC gels with lipid-anchored cRGD (Fig. 3j).

As a demonstration of how the LINC platform can be tuned for different types of tissue culture applications, we grew human hepatic progenitor organoids (HOs) in a stiffer gel (G' ~ 1000 Pa) with or without lipid-presented cRGD (1.5 mM) and physically entrapped laminin (1 mg/mL), as these conditions are reported to support hepatic organoid culture[46,48]. The HOs grown with both laminin and cRGD showed high viability, expression of epithelial markers (E-cadherin), and maintenance of proliferation (Ki67+) (Fig. S17a, b). Consistent with previous reports, we found laminin necessary for HO culture within LINC gels[46], while cRGD was dispensable (Fig. S17a, c). Nevertheless, spheroid formation was significantly enhanced when both cRGD and laminin were included in the LINC gels (Fig. S17c). Taken together, these data demonstrate that LINC Dynamic gels are cytocompatible and modular to support the culture of different human cell types.

Programming macroscale and nanoscale dynamics in LINC gels

Next, we sought to program the nanoscale dynamics in LINC gels by leveraging our control over the physicochemical properties of the self-assembled liposomes. Thus far, all LINC gel formulations consisted of liposomes with exclusively unsaturated lipids. Lipid tail saturation is a well-known factor influencing the characteristics of lipid bilayers[4]. We hypothesized that saturated lipids would have slower membrane mobility due to their denser packing, offering a means to control both macroscale viscoelasticity and nanoscale ligand mobility. To demonstrate, we designed liposomes with exclusively saturated lipids or mixed liposomes with both saturated and unsaturated lipids (Fig. 4a).

At physiological conditions, saturated liposomes exist in a solid-like gel phase with restricted bilayer fluidity[4]. As expected, the fully saturated liposomes displayed lower mobility compared to fully unsaturated liposomes, as confirmed by LAURDAN/ACDAN membrane fluidity measurements and differential scanning calorimetry (DSC) (Figs. 4b and S18). To characterize individual lipid-level dynamics, we used time-correlated single-photon counting (TCSPC) fluorescence anisotropy decay to study the relative movement of fluorescently labeled lipids within liposomes used in different gel conditions. When excited by a polarized incident light, the emission from the lipid-bound fluorescent probes initially retains the polarization of the excitation source. This emission polarization decays in a lipid-mobility-dependent manner as the lipid-anchored fluorophores move. Therefore, the decay in fluorescence anisotropy (i.e., reduction in emission polarization) over time is dependent on the dynamics of the local environment[49]. TCSPC revealed that the fluorescence anisotropy decay in the LINC Saturated liposomes was notably slower than in LINC Unsaturated, with a slower initial decay and a higher residual anisotropy (Figs. 4c and S19). Taken together, the LAURDAN/ACDAN and TCSPC data confirm that lipid movement is restricted within the LINC Saturated liposomes relative to the LINC Unsaturated liposomes.

We hypothesized that this slower lipid mobility would also result in slower stress relaxation at the larger network-level length scale when crosslinking ligands were tethered to saturated lipids. Consistent with this idea, changing tail saturation resulted in minor differences in frequency dependence for the storage modulus with notable changes in loss modulus (Fig. 4d). This indicates distinct relaxation processes within the LINC Unsaturated and Saturated networks, which we attribute to differences in lipid mobility due to the more restricted movement of saturated lipids compared to unsaturated lipids.

Interestingly, while $t_{1/2}$ was significantly greater for LINC Saturated gels compared to stiffness-matched LINC Unsaturated gels (Fig. 4e, 10.3 vs ~1 h, respectively), the stress relaxation profile was not uniformly slowed. Instead, at shorter times (less than ~5 min) the stress relaxation occurred more rapidly in the LINC Saturated gels. For example, the time required to relax 10% of the applied stress was more than an order of magnitude faster for LINC Saturated compared to LINC Unsaturated (Figs. 4e and S20, 5 vs 183 s, respectively). We hypothesize that the initial rapid relaxation may be due to the reduced random lipid motion caused by inherent thermal energy, which may enable greater directional bias of early lipid movement upon application of a directional stress. Future experimentation will be required to evaluate this idea and identify the mechanisms responsible for initial rapid network relaxation. At longer times, the expected slower $t_{1/2}$ is

https://doi.org/10.1038/s41467-026-77268-8

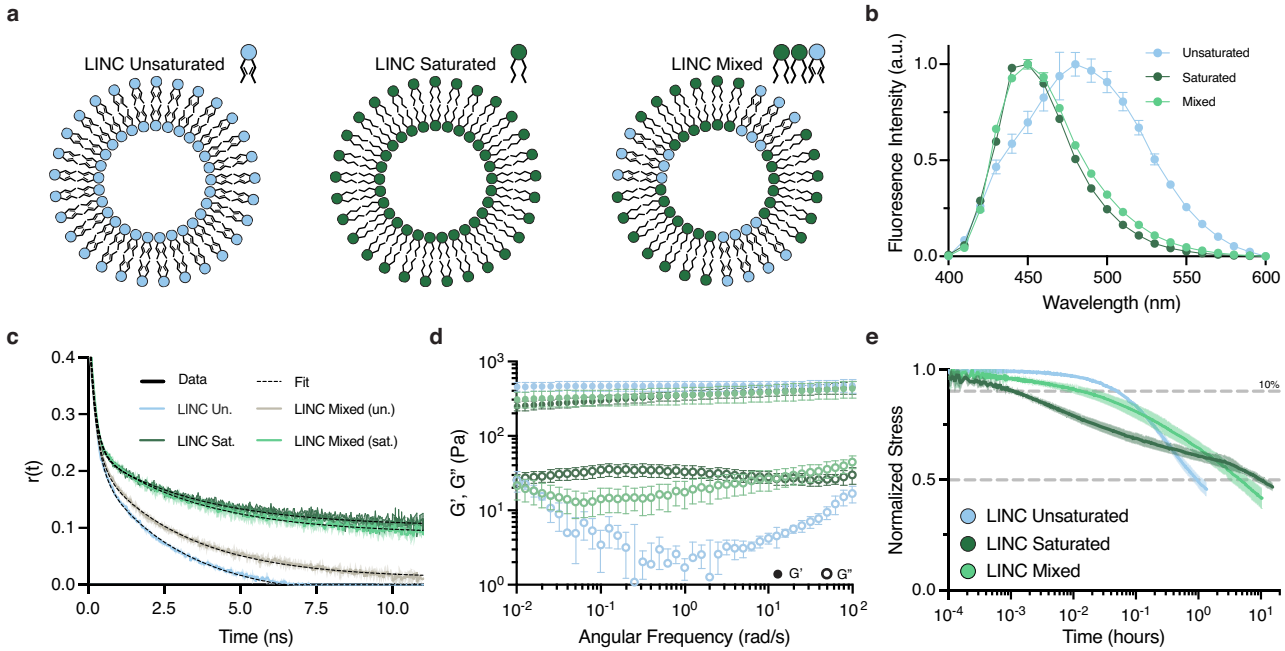


Fig. 4 | Lipid saturation can program nanoscale and macroscale LINC gel dynamics. All conditions contain dynamic crosslinks (HA-benzaldehyde + liposome-hydrazine). **a** Schematic of liposomes composed of unsaturated, saturated, or a 1:2 mix of unsaturated and saturated lipids. **b** LAURDAN fluorescence spectra of LINC Unsaturated, Saturated, and Mixed gels ($N = 3$ independent replicates, mean ± standard deviation). **c** Time-resolved fluorescence anisotropy decay in liposomes composed of unsaturated, saturated, or 1:2 unsaturated:saturated mix. In the mixed liposomes, separate measurements were taken with labeled unsaturated or saturated lipids ($N = 3$ independent replicates, mean ± standard deviation. Fits are two-term exponential decays). **d** Oscillatory rheology frequency sweep of LINC Unsaturated, Saturated, and Mixed gels. $N = 6$ for LINC Unsaturated and Saturated, $N = 7$ for LINC Mixed. Data are mean ± standard deviation. **e** Stress relaxation of LINC Unsaturated, Saturated, and Mixed gels ($N = 6$ for LINC Unsaturated and Saturated, $N = 7$ for LINC Mixed, mean ± standard deviation). Source data are provided as a Source data file.

observed, presumably due to the lower membrane fluidity that restricts long-range lipid motion.

To further characterize the differences in relaxation behavior, we fit the data using a Generalized Maxwell standard linear solid (SLS) model with one or two spring-dashpot pairs (Fig. S21)[50]. Both the one- and two-term SLS models fit the experimental data well for LINC Unsaturated gels ($R^2 = 0.996$ and 0.999, respectively). In contrast, the two-term SLS model achieved higher correlation with the LINC Saturated data compared to the one-term model, indicating an additional relaxation mode for these materials (one-term $R^2 = 0.876$, two-term $R^2 = 0.982$), resulting in two characteristic relaxation times. Notably, the faster characteristic relaxation time ($\tau_{\varepsilon 1}$) of LINC Saturated gels is comparable to values obtained from fitting tissue stress relaxation data with the same two-term SLS model, demonstrating that the LINC Saturated gels approach tissue-like kinetics at short time scales despite the longer $t_{1/2}$ ($\tau_{\varepsilon 1}$ of 59.4 s for LINC Saturated vs 3.7–218.2 s for a range of different reported tissues, Table S3)[1,42]. Thus, this hierarchical design of nanoscale self-assembly within a macroscale polymer network enables the programming of complex viscous behavior such as a bimodal stress relaxation profile.

We reasoned that combining unsaturated and saturated lipids within individual liposomes would enable us to control the macroscale stress relaxation profile and nanoscale ligand dynamics separately by selecting which lipid phase the respective ligands are presented from. For mixed liposomes (33% Unsaturated, 67% Saturated lipids), self-assembly into discrete lipid domains with high and low mobility within single liposomes is expected to occur. DSC confirmed that mixed liposomes exhibit two phases, indicative of intraparticle lipid phase separation (Fig. S18). We designed the liposomes to present crosslinking ligands from the more mobile unsaturated lipids, while the less mobile saturated lipids presented the cell-adhesive ligands. This enables the modular design of macroscopic stress relaxation profile and nanoscale ligand mobility within one gel, where we use one population of lipids for network crosslinking and a second population for cell adhesion. As an estimate of membrane fluidity in the saturated domains of LINC Mixed gels, the fluorescence of LAURDAN (which has a long, saturated acyl tail) was comparable to LINC Saturated gels (Fig. 4b). Additionally, TCSPC fluorescence anisotropy showed comparable anisotropy decays for labeled lipids in LINC Mixed compared to their unmixed controls, i.e., saturated lipids in LINC Mixed had decay profiles similar to LINC Saturated, while unsaturated lipids had more rapid decay profiles for both LINC Mixed and LINC Unsaturated (Figs. 4c and S19). These data suggest that saturated and unsaturated lipids may spatially separate into distinct domains within the Mixed liposomes, enabling them to have similar local nanoscale mobility as in unmixed liposomes.

We then assessed the macroscopic network viscoelastic properties of LINC Mixed gels with unsaturated lipids used as crosslinking points. Interestingly, while the storage modulus for LINC Mixed gels had a plateau frequency response similar to both LINC Unsaturated and Saturated gels, the loss modulus had distinct features (Fig. 4d). Although the LINC Unsaturated and Mixed gels are both crosslinked through unsaturated lipids, the Mixed liposomes also include 67% saturated lipids, which may restrict the available diffusion length of the unsaturated crosslinking lipids, resulting in distinct relaxation modes between the two gels. In support of this, the stress relaxation rate at both short and long time-scales was intermediate to the LINC Unsaturated and Saturated gels (10% and 50% relaxation at 65 s and 5.3 h, respectively) (Figs. 4e and S20). As before, we fit the LINC Mixed relaxation data using one- and two-term Maxwell SLS models. The two-term model achieved a notably better fit with the experimental data (one-term $R^2 = 0.876$, two-term $R^2 = 0.982$), with characteristic

https://doi.org/10.1038/s41467-026-77268-8

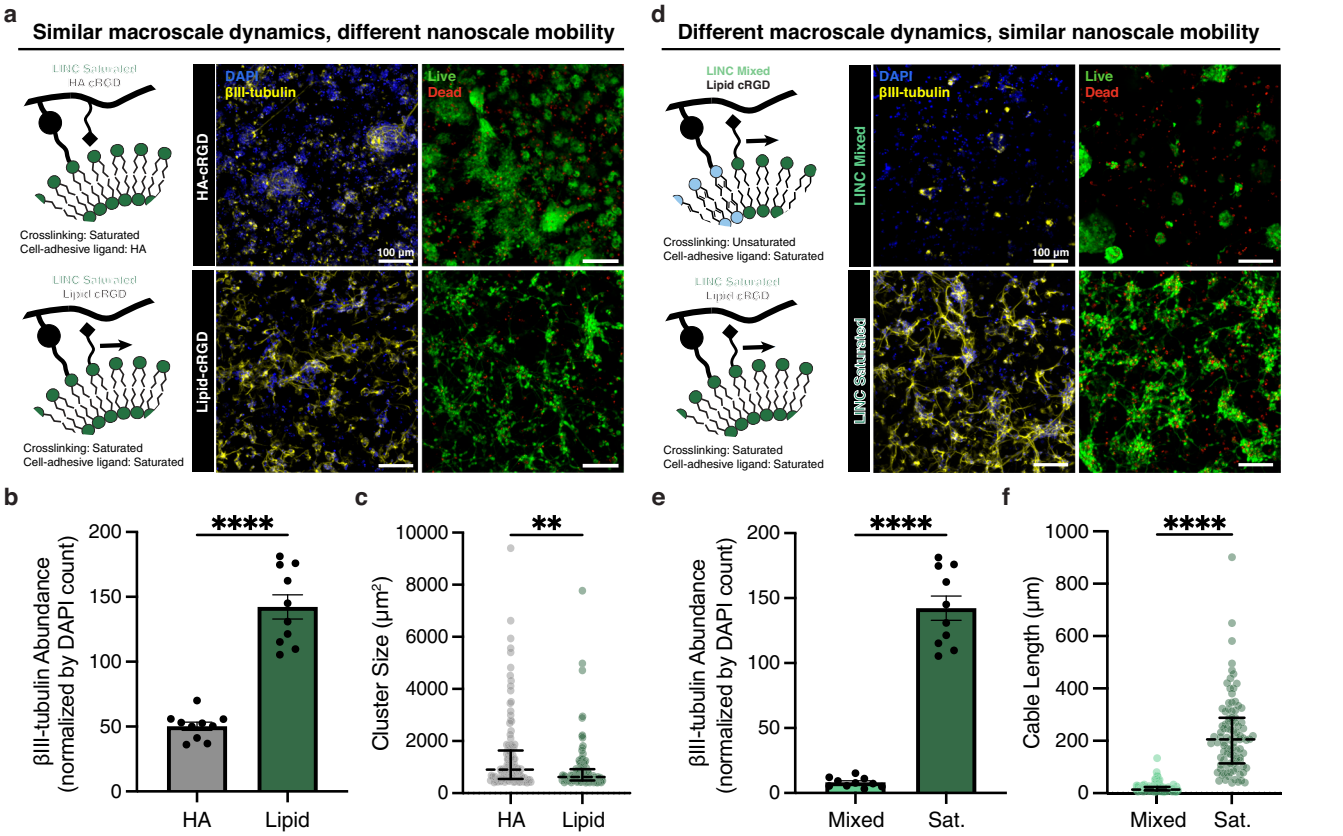


Fig. 5 | LINC gel design reveals that hNPCs respond differentially to macroscale and nanoscale dynamics. Hydrogel formulations are DCC crosslinked, 400 Pa LINC Saturated or LINC Mixed gels, as shown in Fig. 4. **a** Representative fluorescence images of hNPCs encapsulated as single cells in LINC Saturated gels with either lipid- or HA-anchored cRGD after 7 days of culture with labeled nuclei (DAPI, blue) and neuritic extensions (βIII-tubulin, yellow). Scale bar is 100 μm. **b** Quantification of βIII-tubulin area normalized by DAPI count in LINC Saturated HA- or lipid-presented cRGD. ($N = 3$ replicate hydrogels, $n = 5$ fields of view, mean ± standard deviation. ****$p < 0.0001$, 2-way ANOVA with Tukey's multiple comparisons test.) **c** Quantification of hNPC cluster size. ($N = 3$ replicate hydrogels, $n = 3$ fields of view. Data points are individual cell clusters. Bars are medians with interquartile range. **$p = 0.0055$, Kruskal-Wallis with Dunn's multiple comparison test.) **d** Representative fluorescence images of hNPCs encapsulated as single cells in LINC Saturated and Mixed gels with lipid-anchored cRGD after 7 days of culture with labeled nuclei (DAPI, blue) and neuritic extensions (βIII-tubulin, yellow). Scale bar is 100 μm. **e** Quantification of βIII-tubulin area normalized by DAPI count in LINC Saturated and Mixed with lipid-presented cRGD. ($N = 3$ replicate hydrogels, $n = 5$ fields of view, mean ± standard deviation. ****$p < 0.0001$, 2-way ANOVA with Tukey's multiple comparisons test.) **f** Quantification of hNPC neurite cable length in lipid-anchored-cRGD LINC gels. ($N = 3$ replicate hydrogels, $n = 3$ fields of view. Data points represent single cells with traceable neurites. Bars are medians with interquartile range. ****$p < 0.0001$, Kruskal-Wallis with Dunn's multiple comparison test). Source data are provided as a Source data file.

relaxation times intermediate to the LINC Unsaturated and Saturated gels (Fig. S21, Table S3).

Taken together, our data show we can modulate the intraparticle lipid composition to control the macroscopic network stress relaxation dynamics while maintaining comparable nanoscale mobility of the bioactive ligand-presenting saturated lipids. The result is a LINC Mixed gel with similar nanoscale ligand dynamics to the LINC Saturated gels, but significantly differing macroscale viscoelasticity.

Human neural progenitor cells respond to both macroscale and nanoscale network dynamics

We next used this system to investigate the consequences of both macroscale stress relaxation and nanoscale cell-adhesive ligand mobility on hNPC morphology (Fig. 5). hNPCs were encapsulated as single cells to increase their cellular surface contact area with the engineered matrix and to decrease potential confounding signaling from cell-cell interactions inherent to cellular spheroids. The bioactive cRGD ligand was conjugated to either the HA biopolymer, a common method of ligand presentation, or saturated lipids in either the LINC Saturated or Mixed gels. Bioactive ligand presentation was found to have no impact on macroscale viscoelasticity for any LINC gel formulation (Fig. S22). In all formulations, liposome size, liposome concentration, HA concentration, HA benzaldehyde functionalization, gel stiffness, and total cRGD concentration were kept constant (Tables S1 and S2).

After encapsulation within the LINC gels, hNPCs were cultured for 7 days and then analyzed for development of βIII-tubulin-positive neuritic projections and overall morphology (Fig. 5). To evaluate the role of nanoscale cell-interactive ligand mobility within gels of identical macroscale viscoelasticity, hNPCs were cultured in LINC Saturated gels with the bioactive cRGD fixed either to the HA biopolymer or to individual lipids within the saturated liposomes (Fig. 5a–c). When the cRGD ligand was fixed to the HA biopolymer, hNPCs displayed modest βIII-tubulin expression with neurites mostly restricted to large cellular spheroids with limited extension into the surrounding matrix (Fig. 5b, c). These spontaneously forming cellular aggregates are commonly referred to as neurospheres, and this observation is consistent with previous reports that NPCs cultured in gels with longer $t_{1/2}$ display increased neurosphere formation[51]. Interestingly, when the presentation of the cRGD ligand was moved to the liposomes in LINC Saturated gels, we observed a dramatic increase in βIII-tubulin expression (Fig. 5b). In these gels, the hNPCs primarily remained as single cells (Fig. 5c) with long, extended neurites averaging ~200 microns (Fig. 5a,

f). Similarly, the relative mRNA expression of *TUBB3*, which encodes the βIII-tubulin protein, was significantly increased in cells encapsulated in LINC Saturated gels with lipid-presented cRGD compared to HA-presented cRGD (Fig. S23). These results are consistent with two-dimensional lipid bilayer studies of nanoscale ligand mobility, where cell-interactive ligand presentation via high viscosity membranes enhances cell receptor engagement[52,53]. Doping in uncrosslinked saturated liposomes with or without lipid-cRGD into HA hydrogels of similar stiffness resulted in limited viability of hNPCs (Fig. S24). These data suggest that lipid-anchored cRGD must be crosslinked into a LINC gel network to allow cells to generate sufficient cytoskeletal tension to avoid anoikis[54].

One possible driver of these morphological differences may be an enhanced ability to cluster the ligand in the lipid-cRGD conditions due to enhanced ligand mobility. Integrin clustering into local high-density regions is known to facilitate downstream mechanosignaling that alters the cellular cytoskeleton, resulting in neurite outgrowth[16,47,55]. To demonstrate that simply increasing the ligand density in gels with immobile ligands is not sufficient to initiate robust downstream morphological effects, we encapsulated single hNPCs in LINC Saturated gels with 3.3 mM cRGD (i.e., more than double the 1.5 mM cRGD used previously). Despite the higher ligand density, hNPCs still formed large clusters with limited neuritic extension into the gels (Fig. S25). These data suggest that a higher density of relatively immobile ligands is not sufficient to replicate the morphological outcomes observed in gels with more mobile integrin ligands. Thus, for the stress relaxation profile of the LINC Saturated gels, the local nanoscale mobility of bioactive ligands within the three-dimensional network significantly impacts cell phenotype.

Previous work indicates that integrin signaling in stress-relaxing hydrogels influences hNPC fate acquisition and morphological response through cytoskeleton-dependent, actin-mediated mechanosignalling[15,56,57]. To investigate if altered cytoskeletal dynamics contribute to the different cell morphologies observed in gels with more mobile or immobile integrin ligands, we cultured hNPCs in LINC Saturated gels with cRGD (1.5 mM) presented on the lipids (i.e., more mobile) or HA backbone (i.e., less mobile) in the presence of small-molecule inhibitors of actin organization and actomyosin force generation (Fig. S26). If the observed differences in hNPC response between gels with differing ligand presentations are mediated by actomyosin-dependent organization and/or contractility, pharmacologically perturbing these pathways is expected to diminish differences in neurite outgrowth between conditions. Similar to previous reports, βIII-tubulin abundance and neurite outgrowth were reduced to similar levels in both LINC gel conditions when cultured with latrunculin A, which disrupts actin polymerization (Fig. S26A–C). These data suggest that actin polymerization into organized bundles is a necessary requirement for hNPC neurite extension in LINC gels[15]. In contrast, βIII-tubulin abundance and neurite outgrowth increased upon inhibition of actomyosin contractility using either blebbistatin or Y-27632 regardless of ligand presentation (Fig. S26A–C). Blebbistatin is an inhibitor of myosin II, the primary motor protein responsible for actin force generation; and Y-27632 is an inhibitor of ROCK, an upstream kinase that enhances actin stability and myosin II activity. These data demonstrate that reduced actomyosin contractility can increase neurite extension. Together, these findings suggest that gels with more mobile integrin ligands may reduce actomyosin contractility compared to gels with similar bulk matrix dynamics but less mobile ligands, leading to enhanced neurite outgrowth. Interestingly, previous work showed no changes in hNPC βIII-tubulin abundance upon blebbistatin treatment in slow or non-relaxing gels, but an increase in fast-relaxing gels[15]. The similar blebbistatin-response here for both LINC Saturated gels suggests that their initially rapid stress relaxation rates may be critical in regulating actin organization and neurite outgrowth. Collectively, these results highlight the importance of future mechanistic studies using materials with control of matrix dynamics across multiple length and time scales.

Finally, to explore the effect of macroscale viscoelasticity in gels of similar nanoscale dynamics on hNPC phenotype, we cultured hNPCs in LINC Saturated and Mixed gels with the cRGD ligand presented on saturated lipids in both conditions (Fig. 5d–f). While both cultures remained primarily as single cells, LINC Mixed gels did not support the appreciable expression of βIII-tubulin (Fig. 5e), nor the extension of neuritic projections (Fig. 5f). Notably, the LINC Mixed gels display a faster $t_{1/2}$ than the LINC Saturated gels, but lack their initial rapid relaxation (Fig. 4e). This distinct morphological response to different stress relaxation profiles despite similar ligand presentation indicates that the initial rate of network stress relaxation is at least as impactful as the oft-reported $t_{1/2}$ for the LINC system. Taken together, these results highlight the context-dependent effects of both macroscopic stress relaxation dynamics and nanoscale ligand mobility and emphasize the critical need for hydrogels with programmable control of network dynamics across multiple length scales.

Here we introduce the use of self-assembled lipids as dynamic structural elements in engineered hydrogels. Crosslinking through individual, mobile lipids within liposomes provides an approach to control stress relaxation by leveraging bond mobility. With equivalent crosslinking chemistries, lipid network crosslinked hydrogels show 20-fold faster stress relaxation than polymer-only gels. We demonstrate that liposome surface modification, lipid saturation, and mixed-phase lipid membranes provide control over the short and long timescales of stress relaxation. Lipid-bound ligand presentation is tuned independently of viscoelasticity through these same design principles. Finally, we demonstrate the importance of this hierarchical control by showing human neural progenitor cells exhibit distinct morphologies in response to macroscale stress relaxation depending on the nanoscale dynamics of ligand mobility. These results motivate future biophysical studies of the molecular pathways and mechanisms that enable cells to respond to different time-scales and length-scales of hierarchical network dynamics, and provide a platform to do so. While this work focused on morphological assessment of hNPCs, future studies can leverage the LINC platform to explore the effects of these properties on functional outcomes in disease-specific contexts.

Looking ahead, the large body of literature on liposome formulations suggests that this class of materials can have a large design space to explore structure-function relationships to achieve a broad range of multi-length-scale dynamics. For instance, the morphological state of the lipid particles within the LINC gels may be tunable, which may provide another route to influence nanoscale lipid mobility and macroscale viscoelasticity. The LINC hydrogel strategy should be compatible with other chemically modifiable biopolymers, allowing for future application-specific designs of self-assembled lipids with covalent polymer crosslinks. While here the liposomes were used solely as dynamic structural elements, they could simultaneously be exploited for their more traditional roles as drug delivery vehicles or extracellular vesicle signals[23–26,28,58]. Additionally, self-assembled lipids within other hydrogel systems have been shown to be lubricating[59], enhance water retention in flexible sensors[60], and serve as tunable reservoirs for drug release[61]. While we did not explore these properties here, we hypothesize LINC gels may show similar characteristics. Many of these potential future applications will require characterization of the LINC gel platform in vivo, which is particularly important given the broad range of biocompatibility displayed by different lipids[62]. Overall, this work establishes LINC hydrogels as a versatile system using liposomes as intentional structural elements with programmable control over both macroscale and nanoscale dynamics.

Methods

Approval for this study was obtained from the Stanford Institutional Review Board, and informed consent was obtained from all donors.

Lipids

Lipid	Vendor
DOPC	Broadpharm BP-25710
DOPE-mal	Broadpharm BP-28874
18:1 DBCO PE	Avanti Polar Lipids 870129
DSPC	Broadpharm BP-25623
DSPE-mal	Broadpharm BP-26159
16:0 DBCO PE	Avanti Polar Lipids 870128
16:0 NBD PE	Avanti Polar Lipids 810144
18:1 NBD PE	Avanti Polar Lipids 810145
18:1 Cyanine 5.5 PE	Avanti Polar Lipids 810336
18:1 Cyanine 7.0 PE	Avanti Polar Lipids 810337

Statistical analysis

All statistical analysis and data visualization was performed using GraphPad Prism. Specific statistics tests are listed in the figure caption where they appear with replicate information. All data are mean ± standard deviation unless stated otherwise.

HA benzaldehyde synthesis

HA Benzaldehyde with a 20% modification was synthesized as previously described[15]. First, HA is modified with an alkyne group via a carbodiimide reaction to form the intermediate HA-Alkyne. 100 kDa HA (sodium hyaluronate, LifeCore Biomedical) is fully dissolved at 1 wt % in 2-(N-morpholino)ethanesulfonic acid (MES) buffer [0.2 M MES hydrate (Sigma) and 0.15 M NaCl in Milli-Q water (pH 4.5)]. Then, 3 equivalence propargylamine (Sigma) per HA dimer unit was added, and the solution was adjusted to pH 6.0 with NaOH. N-hydroxysuccinimide (3 eq., Thermo Fisher Scientific) was then added as a powder. Immediately after, 3 eq. 1-ethyl-3-(3-dimethylaminopropyl)carbodiimide hydrochloride (EDC) (Sigma) was added as a powder, and the reaction was stirred overnight at room temperature (RT). The reaction was dialyzed against Milli-Q water for 3 days, filtered, lyophilized, and stored at −20 °C.

The HA-Alkyne was then reacted with an azidobenzaldehyde molecule via a copper-catalyzed azide-alkyne click chemistry reaction to form HA Benzaldehyde (HA-BZA). The lyophilized HA-alkyne was dissolved in 10x phosphate-buffered saline [PBS; 81 mM sodium phosphate dibasic, 19 mM sodium phosphate monobasic, and 60 mM sodium chloride in Milli-Q water (pH 7.4)] with β-cyclodextrin (1 mg/ml; Sigma-Aldrich) at 1 wt%. The dissolved HA-alkyne was degassed under nitrogen for 30 min. Sodium ascorbate (0.18 eq., Sigma-Aldrich) and copper (II) sulfate pentahydrate (0.0096 eq., Sigma-Aldrich) were dissolved in Milli-Q water and degassed under nitrogen for 30 min prior to adding them to the HA-alkyne solution. 4-Azidobenzaldehyde (3 eq., Santa Cruz Biotechnology) was dissolved in anhydrous DMSO and added to the HA-Alkyne, sodium ascorbate, and copper (II) sulfate pentahydrate solution. The reaction was stirred for 24 h at RT. Then, an equal volume of EDTA was added for 1 h to chelate the copper (50 mM, pH 7.0, Thermo Fisher Scientific). The reaction was dialyzed against Milli-Q water for 3 days, filtered, lyophilized, and stored at −20 °C.

For cRGD functionalization, HA-BZA was further reacted with Cyclo(-RGDfk) (MedChemExpress) to form HA-BZA cRGD. The same EDC/NHS reaction as used to prepare the HA-alkyne was used with 3 eq of c(-RGDfk) per HA dimer unit. ^{1}H NMR spectra were recorded using nuclear magnetic resonance (NMR) spectroscopy (Varian Inova, 600 MHz) using deuterated D_2O as a solvent.

HA hydrazine synthesis

First, N-(3-azidopropyl)-2-hydrazineylacetamide was synthesized as previously described[63]. Briefly, tri-Boc-hydrazinoacetic acid (1 eq.), azidopropylamine (1.3 eq.), 1-ethyl-3-(3-dimethylaminopropyl)carbodiimide (1.3 eq.) (EDC), and 4-dimethylaminopyridine (0.2 eq.) were dissolved in methylene chloride (DCM) and stirred overnight. Excess solvent was removed using a rotary evaporator under reduced pressure, and the remaining product was purified via silica gel chromatography. The Boc-protected product was then dissolved in a 1:1 mix of DCM:trifluoroacetic acid (TFA) for 4 h to deprotect and precipitated in ether to form an oily yellow solid. Next, HA modification occurred in the same manner as for HA Benzaldehyde, as described above, except the synthesized N-(3-azidopropyl)-2-hydrazineylacetamide was used in place of 4-Azidobenzaldehyde. 1 eq. of propargylamine, EDC, NHS, and -(3-azidopropyl)-2-hydrazineylacetamide were used per HA dimer unit. ^{1}H NMR spectra were recorded using nuclear magnetic resonance (NMR) spectroscopy (Varian Inova, 600 MHz) using deuterated D_2O as a solvent.

HA tetrazine and HA norbornene synthesis

HA was modified with tetrazine or norbornene as previously described[15]. Unmodified HA (100 kDa, LifeCore Biomedical) was fully dissolved in 0.1 M MES buffer (pH 7) at 1 wt%. Then, 1-hydroxybenzotriazole hydrate (2 eq. per HA dimer unit; Sigma-Aldrich) was added and dissolved for 15 min. Separately, tetrazine amine (2 eq. per HA dimer unit; Conju-Probe) or norbornene amine (2 eq. per HA dimer unit; TCI America) were dissolved in acetonitrile (MeCN) mixed with deionized water (5:1). EDC (2 eq) was added as a powder and allowed to dissolve. The mixture was added dropwise to the dissolved HA over 30 min and reacted overnight at room temperature. The reaction mixture was dialyzed for 1 day against a 10% MeCN solution, followed by 3 days against Milli-Q water. The resulting product was then sterile-filtered, lyophilized, and stored at -20 °C. ^{1}H NMR spectra was recorded using NMR spectroscopy (Varian Inova, 600 MHz) using deuterated D_2O as a solvent.

SH-PEG-hydrazine synthesis

SH-PEG2k-NH_2 was dissolved in dimethylformamide (DMF) at 75 mg/mL. Separately, tri-Boc-hydrazinoacetic acid (Sigma, 3 eq.) in equal volume DMF, 4-methylmorpholine (NMM, Sigma, 5 eq.), and HATU (Sigma, 3 eq.) were added sequentially, with 15 min in between each. The tri-Boc-hydrazinoacetic acid-containing solution was let stir for 1 h at room temperature. Then, the SH-PEG-NH_2 (1 eq.) was added dropwise to the tri-Boc-hydrazinoacetic acid mixture at roughly 1 mL / min and left to react for 20–24 h at RT. The reaction was precipitated in ice-cold diethyl ether 3× and dried overnight under nitrogen gas and subsequently dried under vacuum for 3 days. The collected pellet was dissolved in a solution of 50:50 DCM:TFA for 1 h to remove the Boc group. The product was again precipitated 3× in diethyl ether and dried. Of note, deprotection times longer than 1 h led to inconsistent results. Though we did not confirm it, we suspect this is due to TFA-mediated cleavage of the amide bond that has been reported in similar hydrazine-containing molecules[64]. ^{1}H NMR spectra were recorded using nuclear magnetic resonance (NMR) spectroscopy (Varian Inova, 600 MHz) using deuterated D_2O as a solvent.

SH-PEG-norbornene synthesis

First, SH-PEG2k-NH_2 was dissolved at approximately 200 mg/mL in anhydrous DCM. Then, 4-Dimethylaminopyridine (1 eq. to NH_2 DMAP, Sigma-Aldrich) and exo-5-Norbornenecarboxylic acid (6 eq., Sigma-Aldrich) were added as powders. After dissolving, EDC (6 eq.) was added as a powder. The mixture was degassed under nitrogen for 20 min and the reaction proceeded for 24 h at 4 °C in the dark. The reaction was precipitated in ice-cold diethyl ether 3× and dried overnight under nitrogen gas and subsequently dried under vacuum for

3 days. Finally, the dried product was dissolved in Milli-Q water, filtered through a 0.22 μm filter, and lyophilized prior to use. ^{1}H NMR spectra were recorded using nuclear magnetic resonance (NMR) spectroscopy (Varian Inova, 600 MHz) using deuterated D_2O as a solvent.

Liposome fabrication

All liposomes were prepared using a standard thin film hydration and sonication method. Briefly, lipids in chloroform were mixed at the desired ratios (Table S1) and dried under nitrogen gas, then left under vacuum overnight to remove excess chloroform. The resulting lipid films were hydrated in PBS for 10 min with slight agitation. This solution was then sonicated until ~100 nm diameter particles were formed. For liposome formulations containing saturated lipids, this process was done at 70 °C, above the highest reported transition temperature (T_m) of the lipids being used. As the used unsaturated lipids are above their T_m at room temperature, no heating was required.

Once 100 nm particles were achieved via sonication, 1.25 eq. of the crosslinking linker (SH-PEG2k-Hydrazine or SH-PEG2k-Norbornene) was added for 1 h at 37 °C for functionalization. For PEGylated liposomes, the desired ratio of SH-PEG2k-Hydrazine to SH-mPEG was mixed before addition to the liposome solution (Table S1). Lastly, the functionalized particles were purified using 100 kDa Amicon spin filter units (Millipore Sigma). Purification consisted of 3 PBS washes followed by concentrating to a final concentration of 0.17 M, or approximately 133 mg lipids/mL PBS, assuming no loss in the fabrication process. Liposome size was verified via dynamic light scattering (DLS).

Hydrogel formation

For HA-HA gels, all HA conditions were dissolved at 1 wt% in 1x PBS. Once dissolved, the complementary HAs were mixed at a 1:1 volume ratio and hydrogels spontaneously formed.

For LINC Gels, all HA conditions were dissolved at 2 wt% HA in 1x PBS. Once purified, the liposomes were mixed at a 1:1 volume ratio with the functionalized HA for a final concentration of 1 wt% HA. Liposomes were at a final concentration of approximately 67 mg/mL in all hydrogel conditions. Crosslinking occurs spontaneously upon mixing. Liposomes were used within 2 days of fabrication.

Rheological characterization

Rheological measurements were carried out using an ARG2 rheometer (TA Instruments) with a 20 mm, 1° cone-on-plate geometry. Mineral oil was used to seal the hydrogels and prevent dehydration during measurement. Hydrogels were cast at 23 °C, then the temperature was ramped to 37 °C at 2 °C/min. Time sweeps were conducted at 1% oscillatory strain and 1 Hz frequency and allowed to continue until a plateau in moduli was observed. Frequency sweeps were performed from 0.01 to 100 rad/s under 1% oscillatory strain. The reported G′ and G″ values were taken at 6.28 rad/s (1 Hz) from the frequency sweeps. To further characterize the viscoelasticity, stress relaxation measurements were performed under a constant strain of 5%. For Fig. S6, oscillatory strain amplitude sweeps followed by stress relaxation measurements were conducted to evaluate the stability of stress relaxation. First, strain amplitude sweeps from 0.1 to 400% (post-gel failure) were performed, followed by a time sweep at 1% oscillatory strain and 1 Hz frequency for 2 h. Then, stress relaxation measurements were performed under a constant strain of 5%. For stress relaxation in Fig. 2C, data are smoothed with a 2nd-order Gaussian filter over 15 data points due to noise at long times.

Stress sweeps were conducted to determine the failure stress and post-failure recovery of the gels. They were performed with steady-state sensing from 1 Pa to failure, as defined by the measured strain exceeding 1000%, indicative of the geometry rotating freely post-gel failure as all gel conditions fail at strains under 1000%. Reported failure stress values were defined as the last point prior to the above failure definition, also accompanied by an abrupt drop in viscosity. Modulus recovery post-failure was defined by G′ 5 min after the termination of the failure stress measurement using a time sweep at 1% oscillatory strain and 1 Hz frequency. The shear-thinning and self-healing measurements were conducted by performing flow peaks holding for 30 s at alternative low (0.1 s^{-1}) and high (10 s^{-1}) shear rates. All measurements were performed at 37 °C except for the initial time sweeps.

3D printing

Suitability of the LINC Static inks for extrusion-based 3D (bio-)printing was investigated using a MakerGear M2 3D printer equipped with a multi-material extrusion system[65] and a straight 27-gauge dosing needle (inner diameter 210 μm). Gels were cast and allowed to gel within the syringe body for 2 h prior to use. Square-shaped lattice structures (9 × 9 mm^2) consisting of four perpendicular layers and a strand distance 3 mm were printed with constant extrusion rate and a printing speed of 400 mm/min. The prints were imaged with a Leica THUNDER fluorescence microscope.

Förster Resonance Energy Transfer (FRET)

Liposomes were prepared as described above. For each condition, 0.1 mol% of the appropriate fluorescent lipids in chloroform were added during the thin-film drying process. Cy5.5 was used as the donor while Cy7 was used as the acceptor. Donor liposomes were prepared with 0.1 mol% Cy5.5, acceptor liposomes with 0.1 mol% Cy7, and unlabeled liposomes with no fluorophores.

LINC hydrogels were cast as described above into a black, flat-bottom 96-well plate (Costar). Immediately post-casting, the samples were excited at 675 nm (donor excitation) and read at both 720 nm (donor emission) and 790 nm (acceptor emission) every minute. Conditions consisted of (1) donor and acceptor lipids on different liposomes (Donor plus Acceptor), (2) donor liposomes mixed with unlabeled liposomes as a control (Donor), and (3) acceptor liposomes mixed with unlabeled liposomes as a control (Acceptor). The donor-only and acceptor-only conditions contained the same amount of the respective fluorescent lipids as the D + A condition. The reported FRET Ratio is the ratio of the acceptor fluorescence intensity (790 nm) to the donor fluorescence intensity (720 nm) at each time point, normalized to the first time point (t_0). Spectra were collected from 700-850 nm at the end of each measurement (ex 675 nm). PBS-filled wells were used as blanks. Data are smoothed with a 2nd-order Gaussian filter over 5 data points.

Differential scanning calorimetry (DSC)

Liposomes were prepared as described. Liposome solutions in PBS were placed in hermetically sealed TA Instruments T zero pans. An empty pan was used as a reference. Samples were cooled from room temperature to −40 °C, held at −40 °C for 5 min, and heated to −5 °C and held for 5 min. This was repeated twice. Samples were then heated to 23 °C, held for 5 min, heated to 80 °C and held for 5 min, cooled to 23 °C and held. This was repeated twice. Temperatures were ramped at a rate of 2 °C min^{-1}.

ACDAN/LAURDAN

Liposomes were prepared as stated with the addition of 0.05 mol% of either ACDAN (Santa Cruz Biotech) or LAURDAN (Lumiprobe) dissolved in chloroform during the thin film drying process. 40 μL gels or liposomes at the same concentration were cast in a 96-well plate. The samples were excited at 360 nm and readings from 400 to 600 nm were taken 2 h post-casting, once the gels were approximately fully crosslinked. PBS-filled wells were used as blanks.

Time-correlated single-photon counting fluorescence anisotropy

Measurements were conducted using a Horiba Fluorolog-3 Spectrofluorometer with an automated polarizer L-format. Liposomes were

prepared as stated with the addition of 0.2 mol% 18:1 NBD PE (Avanti) or 16:0 NBD PE (Avanti). Measurements were taken at an excitation of 460 nm and emission of 535 nm. G factor correction was conducted with free fluorophore and held constant. IRF correction was performed using 100 nm PS beads (Polysciences). Liposomes were diluted 1:1200 to an approximate concentration of 0.11 mg/mL in PBS. Liposome concentration, slit size, and laser power were all held constant. Fitting was performed using the Horiba DAS-6 analysis software.

Human neural progenitor cell (hNPC) culture

The stemness and differentiation capacity of all hiPSCs was previously validated[66]. Approval for this study was obtained from the Stanford Institutional Review Board, and informed consent was obtained from all donors. hiPSCs were cultured with mTeSR-1 Plus (STEMCELL Technologies) media in monolayer on human embryonic stem cell (hESC)–qualified Matrigel (0.1 mg/mL; Sigma-Aldrich) to maintain their pluripotent state.

hNPCs were differentiated from hiPSCs and cultured as previously described[15]. Briefly, a commercially available dual SMAD inhibition kit (STEMCELL Technologies) was used to differentiate hiPSCs into hNPCs. hiPSCs were expanded to confluency on hESC-qualified Matrigel before being exposed to STEMdiff Neural Induction Medium for 10 days with daily media changes. After, cells were dissociated with cell dissociation solution (Sigma-Aldrich), passaged onto poly-d-lysine (50 μg/mL; Sigma-Aldrich) and laminin (10 μg/mL; Roche) coated plates. At this point, hNPCs were maintained in N3 culture medium consisting of DMEM/F12 (Thermo Fisher Scientific), neurobasal (Thermo Fisher Scientific), N-2 supplement (1%, Thermo Fisher Scientific), B-27 supplement with vitamin A (2%, Thermo Fisher Scientific), GlutaMax (1%, Thermo Fisher Scientific), and Minimal Essential Medium Nonessential Amino Acids (1%, Thermo Fisher Scientific).

hNPC encapsulation

hNPCs were either encapsulated as single cells or formed into spheroids prior to encapsulation. For spheroid encapsulation, hNPCs were dissociated, and about 1.5×10^6 single cells were seeded per well of an AggreWell 800 plate (STEMCELL Technologies) in N3 media. After 48 h, hNPC spheroids of approximately 5,000 cells were then collected, pelleted by centrifugation, and resuspended in a 2 wt% HA-BZA solution. Gels were cast and allowed to gel for 30 min. 750 μL of N3 media was added to each well containing a 10 μL hydrogel. Medium was changed daily.

For single-cell encapsulation, hNPCs were dissociated, filtered through a 70 μm cell strainer, pelleted by centrifugation, and counted. They were then resuspended in a 2 wt% HA-BZA solution at a cell density of 6×10^4 cells/μL, for a final gel concentration of 3×10^4 cells/μL. Gels were cast and allowed to gel for 30 min. 750 μL of N3 media was added to each well containing a 10 μL hydrogel. Medium was changed daily.

Cytoskeletal inhibitors

Latrunculin A (Tocris) was used at 1 μM, blebbistatin (Abcam) at 10 μM, and Y-27632 (Selleck Chemical) at 10 μM. Inhibitors were added to the gels at day 1 and replenished daily.

RNA isolation and qPCR

Hydrogels containing encapsulated hNPCs were collected in Eppendorf tubes and resuspended in TRIzol reagent (Invitrogen) and stored at −80 °C. Samples were thawed on ice and subjected to probe sonication (50% amplitude (25 W), 0.5 s cycles, 30-kHz frequency) to disrupt the remaining gel fragments. Then, mRNA was purified using phenol-chloroform extraction and isopropyl alcoholic precipitation and subsequent 70% ethanol washing. A High Capacity cDNA Reverse Transcription Kit (Applied Biosystems) was used to reverse transcribe 200 ng of mRNA. cDNA was then diluted 10x in nuclease-free water, 6.6 μL of cDNA was mixed with 0.9 μL of forward and reverse primers at 5 μM along with 7.5 μL of Fast SYBR Green Master Mix (Applied Biosystems). Finally, the mixture was run on a StepOnePlus Real-Time PCR System and analyzed using the ΔC_T method. Forward Primer (5′ to 3′): GGCCAAGGGTCACTACACG. Reverse Primer (5′ to 3′): GCAGTCGCA GTTTTCACACTC.

Manual neurite tracing

βIII-tubulin-positive neurites were manually traced and quantified with the SNT toolbox to assess their length and branching complexity[67]. Neurites with a total length less than 5 μm were not traced; otherwise, to the greatest degree possible, all neurites longer than 5 μm were traced in 3D space.

Cell viability

Cell-containing hydrogels were washed with DPBS and incubated with 2 μM calcein acetoxymethyl and 4 μM ethidium homodimer for 20 min at 37 °C. The gels were washed with DPBS and imaged with a confocal microscope (Leica SPE).

Hepatic progenitor organoid generation and passaging in Matrigel

Hepatic organoids were derived from iPSCs using previously reported methods[46]. Human iPSC-derived hepatic progenitor cells were cultured in 50 μL Matrigel domes at 200 cells/μL seeding density within a 24-well plate to generate hepatic organoids. Organoids were passaged every 7 days. To passage organoids, Matrigel domes were incubated for 30 min with 1 mL ice-cold, 5 mM ethylenediamine tetra-acetic acid (EDTA) in PBS to dissociate the gels. The cells were then collected and centrifuged for 5 min at 500 × *g* and treated with 1 mL TrypLE (Thermo Fisher Scientific) for 6 min at 37 °C. Gentle mixing by pipette aspiration every 3 min assisted the organoid dissociation into single cells. The TrypLE was then quenched with 400 μL 40% FBS in PBS, and centrifuged for 5 min at 500 × *g*. The cell pellet was resuspended in hepatic growth medium for cell counting. The desired number of cells were centrifuged for 5 min at 500 × *g* and resuspended in fresh, ice-cold Matrigel solution at 200 cells/μL. The Matrigel domes were incubated for 10 min of gelation at 37 °C, then 700 μL of pre-warmed organoid growth medium was added to each well. Y-27632 (10 μM Cayman Chemical) was added to the medium for the first 2 days. Media was replaced every 2–3 days. To make complete hepatic growth media, RPMI media was supplemented with 1x B27 (Thermo), 250 nM LDN-193189 (Cayman Chemical), 3 μM CHIR99021 (Cayman Chemical), 10 μM A83-01 (Cayman Chemical), 100 ng/mL EGF (Cayman Chemical), 10 ng/mL FGF10 (Cayman Chemical), 20 ng/mL HGF (Cayman Chemical).

Hepatic progenitor organoid culture in LINC gels

HA and liposome stock solutions were prepared as described above. 6 mg/mL laminin-111 (R&D Systems) was premixed with the liposome solution to have a final concentration of 1 mg/mL in LINC gels. Hepatic organoids were released from Matrigel and dissociated into single cells as described above. The desired number of cells were centrifuged for 5 min at 500 × *g* and resuspended in the solution of liposomes and laminin. The gels were cast as previously stated, with a cell seeding density of 2 k/μL. Gels were cast and allowed to gel for 30 min. Following gelation, LINC hydrogels were submerged in organoid passage media (growth media with Y-27632) for 2 days, then changed to growth media with changes every 2–3 days for a week.

Immunocytochemistry (ICC)

Importantly, ICC was performed using Tween-20 as a permeabilization agent instead of Triton X-100, as Triton X-100 disrupts the liposome structure, leading to immediate gel dissociation even post-fixation.

Cell-containing hydrogels were washed with DPBS, fixed in a 4% paraformaldehyde solution for 20 min at 37 °C, followed by 3 washes with DPBS. Then, samples were permeabilized for 1 h at room temperature with 0.1% (v/v) Tween-20 in PBS (PBST) and subsequently blocked with PBS supplemented with 5% (w/v) bovine serum albumin (BSA, Roche), 5% (v/v) goat serum (Gibco), and 0.1% (v/v) Tween-20 for 3 h at room temperature with gentle rocking. Primary antibodies were prepared in PBS with 2.5% (w/v) BSA, 2.5% (v/v) goat serum, and 0.1% (v/v) Tween-20 (antibody dilution solution). Mouse anti-βIII-tubulin was used at a 1:400 dilution (Cell Signaling #4466). Samples were incubated with primary antibodies overnight at 4 °C and then washed with PBS 3 times for 30 min each. Then, secondary antibodies were diluted in antibody dilution solution, added to the samples, and incubated overnight at 4 °C prior to 3 additional PBS washes. Goat anti-mouse Alexa Fluor 488 (Invitrogen) was used at a 1:500 dilution, and diamidino-2-phenylindole (DAPI, 1 μg/mL, Cell Signaling) was included in the secondary antibody solution for nuclear staining. The stained hydrogels were inverted and imaged directly with a confocal microscope (Leica SPE).

Hepatic organoids in gels were fixed with 750 μL of 4% paraformaldehyde (PFA) in DPBS for 15 min. Fixation solution was then removed, and three 10 min washes of DPBS were performed. The gels were incubated in 30% sucrose solution at 4 °C overnight. Gels then embedded into a 1 mL 1:1 ratio mixture of 30% sucrose and Tissue-Tek O.C.T Compound (Sakura Finetek USA, Torrance, CA) into Tissue-Tek Cryomold molds (Sakura Finetek USA, Torrance, CA). After for 24 h incubation at RT, samples were moved onto dry ice for rapid freezing (~ 10 min). The samples were then snap frozen on dry ice and cryo-sectioned into 40 μm sections using a Leica Cryostat instrument.

Sectioned samples were melted at 50 °C for 5–10 min and subsequently washed with DPBS to remove excess O.C.T. The gel sections were circled with lipid-repellent marker pen for further staining. Samples were permeabilized for 1 h with 0.5% v/v Tween-20 in DPBS, then blocked for 3 h in DPBS with 5% v/v goat serum, 0.5% v/v Tween-20, and 5 wt% BSA. Staining was conducted as above, with mouse anti-Ki67 was added at 1:200 (Cell Signaling) and rabbit anti E-Cadherin was added to 1:400 (Cell Signaling) primary antibodies. Samples were mounted to No.1 glass over slides with ProLong Gold Antifade Reagent for 24–48 h at RT in dark. Stained samples were imaged using a confocal microscope (Leica SPE) and analyzed using ImageJ (NIH, v.2.1.0/1.53c).

Reporting summary

Further information on research design is available in the Nature Portfolio Reporting Summary linked to this article.

Data availability

The data generated in this study have been deposited in the Stanford Digital Repository, which can be accessed through the persistent URL and the DOI (https://doi.org/10.25740/mh765ys7343). Source data are provided with this paper.

References

1. Chaudhuri, O., Cooper-White, J., Janmey, P. A., Mooney, D. J. & Shenoy, V. B. Effects of extracellular matrix viscoelasticity on cellular behaviour. *Nature* **584**, 535–546 (2020).
2. Courbot, O. & Elosegui-Artola, A. The role of extracellular matrix viscoelasticity in development and disease. *npj Biol. Phys. Mech.* **2**, 10 (2025).
3. Saraswathibhatla, A., Indana, D. & Chaudhuri, O. Cell–extracellular matrix mechanotransduction in 3D. *Nat. Rev. Mol. Cell Biol.* 1–22 https://doi.org/10.1038/s41580-023-00583-1 (2023).
4. Alberts, B. et al. The lipid bilayer. in *Molecular Biology of the Cell* 4th edn (Garland Science, 2002).
5. Jahnke, K. & Staufer, O. Membranes on the move: the functional role of the extracellular vesicle membrane for contact-dependent cellular signalling. *J. Extracell. Vesicles* **13**, e12436 (2024).
6. Lou, J. & Mooney, D. J. Chemical strategies to engineer hydrogels for cell culture. *Nat. Rev. Chem.* **6**, 726–744 (2022).
7. Álvarez, Z. et al. Bioactive scaffolds with enhanced supramolecular motion promote recovery from spinal cord injury. *Science* **374**, 848–856 (2021).
8. 3D bioprinting of dynamic hydrogel bioinks enabled by small molecule modulators. *Sci. Adv.* https://www.science.org/doi/full/10.1126/sciadv.ade7880?rfr_dat=cr_pub++0pubmed&url_ver=Z39.88-2003&rfr_id=ori%3Arid%3Acrossref.org.
9. Rijns, L., Baker, M. B. & Dankers, P. Y. W. Using chemistry to recreate the complexity of the extracellular matrix: guidelines for supramolecular hydrogel–cell interactions. *J. Am. Chem. Soc.* **146**, 17539–17558 (2024).
10. Li, J. & Mooney, D. J. Designing hydrogels for controlled drug delivery. *Nat. Rev. Mater.* **1**, 1–17 (2016).
11. Hafeez, S. et al. Molecular tuning of a benzene-1,3,5-tricarboxamide supramolecular fibrous hydrogel enables control over viscoelasticity and creates tunable ECM-mimetic hydrogels and bioinks. *Adv. Mater.* **35**, 2207053 (2023).
12. McKinnon, D. D., Domaille, D. W., Cha, J. N. & Anseth, K. S. Biophysically defined and cytocompatible covalently adaptable networks as viscoelastic 3D cell culture systems. *Adv. Mater.* **26**, 865–872 (2014).
13. Sousa, V. et al. Merging natural biopolymers with supramolecular chemistry: emulating the native extracellular matrix's complexity. *ACS Nano* **19**, 29833–29859 (2025).
14. Nelson, B. R. et al. Photoinduced dithiolane crosslinking for multiresponsive dynamic hydrogels. *Adv. Mater.* **36**, 2211209 (2024).
15. Roth, J. G. et al. Tunable hydrogel viscoelasticity modulates human neural maturation. *Sci. Adv.* **9**, eadh8313 (2023).
16. Álvarez, Z. et al. Artificial extracellular matrix scaffolds of mobile molecules enhance maturation of human stem cell-derived neurons. *Cell Stem Cell* **30**, 219–238.e14 (2023).
17. Diba, M. et al. Engineering the dynamics of cell adhesion cues in supramolecular hydrogels for facile control over cell encapsulation and behavior. *Adv. Mater.* **33**, 2008111 (2021).
18. Rijns, L. et al. The importance of effective ligand concentration to direct epithelial cell polarity in dynamic hydrogels. *Adv. Mater.* **36**, 2300873 (2024).
19. Moghaddam, A. S., Dunne, K., Breyer, W., Wu, Y. & Pashuck, E. T. Hydrogels with multiple RGD presentations increase cell adhesion and spreading. *Acta Biomater.* **199**, 142–153 (2025).
20. Rijns, L. et al. Synthetic, multi-dynamic hydrogels by uniting stress-stiffening and supramolecular polymers. *Sci. Adv.* **10**, eadr3209 (2024).
21. Rijns, L. et al. Importance of molecular and bulk dynamics in supramolecular hydrogels in dictating cellular spreading. *Chem. Mater.* **35**, 8203–8217 (2023).
22. Huster, D., Maiti, S. & Herrmann, A. Phospholipid membranes as chemically and functionally tunable materials. *Adv. Mater.* **36**, 2312898 (2024).
23. Shi, L. et al. Extracellular vesicle crosslinkers constructing hydrogels with stress-relaxation and bioactive protein modification. *Adv. Mater. Interfaces* **12**, 2400885 (2025).
24. Zhang, Q. et al. Therapeutic potential of injectable supramolecular hydrogels with neural stem cell exosomes and hydroxypropyl methylcellulose for post-stroke neurological recovery. *Int. J. Nanomedicine* **20**, 2253–2271 (2025).
25. Zhang, X. et al. Artificial apoptotic cells/VEGF-loaded injectable hydrogel united with immunomodification and revascularization functions to reduce cardiac remodeling after myocardial infarction. *Nano Today* **39**, 101227 (2021).

26. Liang, Y. & Kiick, K. L. Liposome-cross-linked hybrid hydrogels for glutathione-triggered delivery of multiple cargo molecules. *Biomacromolecules* **17**, 601–614 (2016).
27. Mouritsen, O. G. Lipids, curvature, and nano-medicine. *Eur. J. Lipid Sci. Technol.* **113**, 1174–1187 (2011).
28. Correa, S., Grosskopf, A. K., Klich, J. H., Hernandez, H. L. & Appel, E. A. Injectable liposome-based supramolecular hydrogels for the programmable release of multiple protein drugs. *Matter* **5**, 1816–1838 (2022).
29. Talló, K., Bosch, M., Pons, R., Cocera, M. & López, O. Preparation and characterization of a supramolecular hydrogel made of phospholipids and oleic acid with a high water content. https://doi.org/10.1039/C9TB01599J (2019).
30. Dessane, B. et al. Nucleotide lipid-based hydrogel as a new biomaterial ink for biofabrication. *Sci. Rep.* **10**, 2850 (2020).
31. Mangiarotti, A. et al. Biomolecular condensates modulate membrane lipid packing and hydration. *Nat. Commun.* **14**, 6081 (2023).
32. Orlikowska-Rzeznik, H., Krok, E., Chattopadhyay, M., Lester, A. & Piatkowski, L. Laurdan discerns lipid membrane hydration and cholesterol content. *J. Phys. Chem. B* **127**, 3382–3391 (2023).
33. Zhang, S., Metelev, V., Tabatadze, D., Zamecnik, P. C. & Bogdanov, A. Fluorescence resonance energy transfer in near-infrared fluorescent oligonucleotide probes for detecting protein–DNA interactions. *Proc. Natl. Acad. Sci. USA* **105**, 4156–4161 (2008).
34. Loura, L. M. S. Simple estimation of Förster Resonance Energy Transfer (FRET) orientation factor distribution in membranes. *Int. J. Mol. Sci.* **13**, 15252–15270 (2012).
35. Rizwan, M., Baker, A. E. G. & Shoichet, M. S. Designing hydrogels for 3D cell culture using dynamic covalent crosslinking. *Adv. Healthc. Mater.* **10**, 2100234 (2021).
36. LeSavage, B. L. et al. Engineered matrices reveal stiffness-mediated chemoresistance in patient-derived pancreatic cancer organoids. *Nat. Mater.* **23**, 1138–1149 (2024).
37. Gilchrist, A. E. et al. Transient competitors to modulate dynamic covalent cross-linking of recombinant hydrogels. *Chem. Mater.* **35**, 8969–8983 (2023).
38. de Paiva Narciso, N. et al. Design parameters for injectable biopolymeric hydrogels with dynamic covalent chemistry crosslinks. *Adv. Healthc. Mater.* **12**, 2301265 (2023).
39. Jencks, W. P. Studies on the mechanism of oxime and semicarbazone formation1. *J. Am. Chem. Soc.* **81**, 475–481 (1959).
40. Zhang, D., Baugh, N. J., de Paiva Narciso, N. & Heilshorn, S. C. Physiological buffer selection alters the mechanics of hydrogels with hydrazone cross-links. *Biomacromolecules* **27**, 3222–3236 (2026).
41. Tabarin, T., Martin, A., Forster, R. J. & Keyes, T. E. Poly-ethylene glycol induced super-diffusivity in lipid bilayer membranes. *Soft Matter* **8**, 8743–8751 (2012).
42. Chaudhuri, O. et al. Hydrogels with tunable stress relaxation regulate stem cell fate and activity. *Nat. Mater.* **15**, 326–334 (2016).
43. Hofer, M. & Lutolf, M. P. Engineering organoids. *Nat. Rev. Mater.* **6**, 402–420 (2021).
44. Fatehullah, A., Tan, S. H. & Barker, N. Organoids as an in vitro model of human development and disease. *Nat. Cell Biol.* **18**, 246–254 (2016).
45. Roth, J. G. et al. Spatially controlled construction of assembloids using bioprinting. *Nat. Commun.* **14**, 4346 (2023).
46. Liu, Y. et al. Engineered hydrogels for organoid models of human nonalcoholic fatty liver disease. *Adv. Sci.* **12**, e17332 (2025).
47. Ananthanarayanan, B., Little, L., Schaffer, D. V., Healy, K. E. & Tirrell, M. Neural stem cell adhesion and proliferation on phospholipid bilayers functionalized with RGD peptides. *Biomaterials* **31**, 8706–8715 (2010).
48. Gjorevski, N. et al. Designer matrices for intestinal stem cell and organoid culture. *Nature* **539**, 560–564 (2016).
49. Amaro, M. et al. Time-resolved fluorescence in lipid bilayers: selected applications and advantages over steady state. *Biophys. J.* **107**, 2751–2760 (2014).
50. Chaudhuri, O. Viscoelastic hydrogels for 3D cell culture. *Biomater. Sci.* **5**, 1480–1490 (2017).
51. Huang, M. S. et al. Viscoelastic N-cadherin-like interactions maintain neural progenitor cell stemness within 3D matrices. *Nat. Commun.* **16**, 5213 (2025).
52. Barcelona-Estaje, E. et al. N-cadherin crosstalk with integrin weakens the molecular clutch in response to surface viscosity. *Nat. Commun.* **15**, 8824 (2024).
53. Bennett, M. et al. Molecular clutch drives cell response to surface viscosity. *Proc. Natl. Acad. Sci. USA* **115**, 1192–1197 (2018).
54. Mei, J. et al. Anoikis in cell fate, physiopathology, and therapeutic interventions. *MedComm* **5**, e718 (2024).
55. Chen, Y.-C. et al. DNA tension assays reveal that force-dependent integrin activation regulates neurite outgrowth in primary cortical neurons. *Biomater. Adv.* **150**, 213431 (2023).
56. Egr1 is a 3D matrix–specific mediator of mechanosensitive stem cell lineage commitment. *Sci. Adv.* https://www.science.org/doi/10.1126/sciadv.abm4646.
57. Musah, S. et al. Substratum-induced differentiation of human pluripotent stem cells reveals the coactivator YAP is a potent regulator of neuronal specification. *Proc. Natl. Acad. Sci. USA* **111**, 13805–13810 (2014).
58. Ma, Y.-H. et al. Biodegradable and injectable polymer–liposome hydrogel: a promising cell carrier. *Polym. Chem.* **7**, 2037–2044 (2016).
59. Lin, W. et al. Cartilage-inspired, lipid-based boundary-lubricated hydrogels. *Science* **370**, 335–338 (2020).
60. Bai, M. et al. Bioinspired adaptive lipid-integrated bilayer coating for enhancing dynamic water retention in hydrogel-based flexible sensors. *Nat. Commun.* **15**, 10569 (2024).
61. Wu, F., Chen, H., Liu, J. & Pang, Y. Generating structurally and functionally programmable hydrogels by biological membrane hybridization. *Nat. Protoc.* 1–32 https://doi.org/10.1038/s41596-025-01247-4 (2025).
62. Lee, Y., Jeong, M., Park, J., Jung, H. & Lee, H. Immunogenicity of lipid nanoparticles and its impact on the efficacy of mRNA vaccines and therapeutics. *Exp. Mol. Med.* **55**, 2085–2096 (2023).
63. Lou, J. et al. Dynamic hyaluronan hydrogels with temporally modulated high injectability and stability using a biocompatible catalyst. *Adv. Mater.* **30**, e1705215 (2018).
64. Dalabehera, N. R., Meher, S., Bhusana Palai, B. & Sharma, N. K. Instability of amide bond with trifluoroacetic acid (20%): synthesis, conformational analysis, and mechanistic insights into cleavable amide bond comprising β-troponylhydrazino acid. *ACS Omega* **5**, 26141–26152 (2020).
65. Pusch, K., Hinton, T. J. & Feinberg, A. W. Large volume syringe pump extruder for desktop 3D printers. *HardwareX* **3**, 49–61 (2018).
66. Roth, J. G. et al. 16p11.2 microdeletion imparts transcriptional alterations in human iPSC-derived models of early neural development. *eLife* **9**, e58178 (2020).
67. Arshadi, C., Günther, U., Eddison, M., Harrington, K. I. S. & Ferreira, T. A. SNT: a unifying toolbox for quantification of neuronal anatomy. *Nat. Methods* **18**, 374–377 (2021).

Acknowledgements

The authors thank Dr. Carla Huerta-López and Dr. Fotis Christakopoulos for their helpful feedback and discussions. Part of this work was performed at the Stanford Nano Shared Facilities, supported by the NSF (ECCS-2026822).

Author contributions

Conceptualization: N.J.B., S.C.H. Methodology: N.J.B., M.S.H., N.P.N., Y.L., D.K., R.S.N. Investigation: N.J.B., M.S.H., N.P.N., J.A.B., D.Z., V.M.D., J.W., Y.L., R.O., D.K., R.S.N. Visualization: N.J.B. Funding acquisition: S.C.H. Supervision: S.C.H. Writing: N.J.B., S.C.H. Manuscript editing: N.J.B., M.S.H., N.P.N., J.A.B., Y.L., D.K., S.C.H.

Funding

This work was supported by the National Science Foundation (NSF), grants DGE-1656518 (N.J.B. and M.S.H.), DMR-2427971 and CBET-2033302 (S.C.H.); the National Institutes of Health (NIH), grants F31-HL175888 (N.J.B.), F31-NS132505 (M.S.H.), K99-HL169844 (R.S.N.), R01 HL173056 and R01 MH137333 (S.C.H.); a Stanford Cardiovascular Institute seed grant (S.C.H.); Stanford Human Performance Alliance grant WTHPA-2024-003 (S.C.H.); Stanford Wu-Tsai Neurosciences Institute grant KPI-001 (S.C.H.); the ARCS Foundation Scholarship (N.J.B.); the PhRMA Foundation Predoctoral Fellowship in Drug Delivery (N.J.B.); the Sarafan ChEM-H O'Leary-Thiry Fellowship (M.S.H.); the Gerald J. Lieberman Fellowship (M.S.H. and N.P.N.); the American Heart Association Predoctoral Fellowship 24PRE1191604 (N.P.N.).

Competing interests

The authors declare no competing interests.

Additional information

Supplementary information The online version contains supplementary material available at https://doi.org/10.1038/s41467-026-77268-8.

Correspondence and requests for materials should be addressed to Sarah C. Heilshorn.

Peer review information *Nature Communications* thanks Di Jia, Yuhong Liu and the other anonymous reviewers for their contribution to the peer review of this work. A peer review file is available.

Reprints and permissions information is available at http://www.nature.com/reprints

Publisher's note Springer Nature remains neutral with regard to jurisdictional claims in published maps and institutional affiliations.

Open Access This article is licensed under a Creative Commons Attribution-NonCommercial-NoDerivatives 4.0 International License, which permits any non-commercial use, sharing, distribution and reproduction in any medium or format, as long as you give appropriate credit to the original author(s) and the source, provide a link to the Creative Commons licence, and indicate if you modified the licensed material. You do not have permission under this licence to share adapted material derived from this article or parts of it. The images or other third party material in this article are included in the article's Creative Commons licence, unless indicated otherwise in a credit line to the material. If material is not included in the article's Creative Commons licence and your intended use is not permitted by statutory regulation or exceeds the permitted use, you will need to obtain permission directly from the copyright holder. To view a copy of this licence, visit http://creativecommons.org/licenses/by-nc-nd/4.0/.

© The Author(s) 2026